

Coupled dimerized alternating-bond quantum spin chains in the distorted honeycomb-lattice magnet Cu₅SbO₆

C. Piyakulworawat,^{1,2} K. Morita,³ Y. Fukumoto,⁴ W. -Y. Hsieh,^{5,6} W. -T. Chen,^{5,7,6} K. Nakajima,⁸ S. Ohira-Kawamura,⁸ Y. Zhao,^{9,10} S. Wannapaiboon,¹¹ P. Piyawongwatthana,⁸ T. J. Sato,^{12,13} and K. Matan^{1,2,*}

¹Department of Physics, Faculty of Science, Mahidol University, Bangkok 10400, Thailand

²Thailand Center of Excellence in Physics, Commission of Higher Education, Bangkok 10400, Thailand

³Department of Physics, Tohoku University, Sendai, Miyagi 980-8578, Japan

⁴Department of Physics and Astronomy, Faculty and Science and Technology, Tokyo University of Science, Chiba 278-8510, Japan

⁵Center for Condensed Matter Sciences, National Taiwan University, Taipei 10617, Taiwan

⁶Taiwan Consortium of Emergent Crystalline Materials,

National Science and Technology Council, Taipei 10622, Taiwan

⁷Center of Atomic Initiative for New Materials, National Taiwan University, Taipei 10617, Taiwan

⁸Materials and Life Science Division, J-PARC Center, Tokai, Ibaraki 319-1195, Japan

⁹Department of Materials Science and Engineering,

University of Maryland, College Park, Maryland 20742, USA

¹⁰NIST Center for Neutron Research, National Institute of Standards and Technology, Gaithersburg, Maryland 20899, USA

¹¹Synchrotron Light Research Institute, 111 University Avenue, Muang, Nakhon Ratchasima 30000, Thailand

¹²Institute for Multidisciplinary Research for Advanced Materials,

Tohoku University, 2-1-1 Katahira, Sendai, Miyagi 980-8577, Japan

¹³Neutron Science Laboratory, Institute for Solid-State Physics,

The University of Tokyo, Kashiwa, Chiba 277-8581, Japan

(Dated: February 16, 2026)

We analyze powder-averaged inelastic neutron scattering and magnetization data for the distorted honeycomb compound Cu₅SbO₆ using a first-order dimer expansion calculation and quantum Monte Carlo simulations. We show that, in contrast to the previously proposed honeycomb lattice model, Cu₅SbO₆ accommodates interacting dimerized spin chains with alternating ferromagnetic-antiferromagnetic couplings along the chain. Moreover, unlike the typical couplings observed in other Cu²⁺-based distorted honeycomb magnets, the spin chains in Cu₅SbO₆ primarily couple through an antiferromagnetic coupling that arises between the honeycomb layers, rather than the expected interchain coupling in the layers. This finding reveals a different magnetic coupling scheme for Cu₅SbO₆. In addition, utilizing x-ray spectroscopy and transmission electron microscopy, we also refine the crystal structure and stacking-fault model of the compound.

I. INTRODUCTION

Dimerized quantum magnets have constituted a fertile ground for exploring a plethora of exotic emergent quantum phenomena in magnetic insulators [1, 2]. The most renowned aspect of such magnets is arguably quantum criticality. One of the quantum phase transitions is achieved in the field-induced Bose-Einstein condensation of magnons realized in several compounds [3–10]. Novel phenomena in the vicinity of a quantum critical point separating a dimerized disordered phase from a long-range ordered phase such as dimensional reduction [11] and longitudinal excitation modes [12] have been observed. When frustration between exchange couplings among orthogonally oriented dimers are present as in the Shastry-Sutherland magnet, several other intriguing effects have been reported including topologically protected chiral edge modes of triplet excitations [13], pressure-induced 4-spin plaquette singlet state [14, 15], field-induced spin-nematic phase [16], incomplete devil's

staircase [17] and crystallization of triplet bound states in magnetization plateaus [18]. Dimerized magnets are built upon spin dimers consisting of a pair of spins interacting with an intra-dimer antiferromagnetic (AFM) exchange coupling. The dimer, for the case of $S = \frac{1}{2}$, exhibits a non-magnetic singlet ground state and degenerate triplet excited states in zero magnetic field which are separated by a finite energy gap. Dimers that interact with each other with a ferromagnetic (FM) exchange coupling in a one-dimensional (1D) network, forming an alternating FM-AFM spin chain, form another distinct class of dimerized magnets. Magnetic materials that are characterized as quasi-1D FM-AFM dimerized spin chains include, as examples, copper nitrate [19], BaCu₂V₂O₈ [20], CuNb₂O₆ [21], (CH₃)₂NH₂CuCl₃ [22], etc.

To our knowledge, the archetypes of the quasi-1D $S = \frac{1}{2}$ alternating FM-AFM dimerized spin chain realized in a *distorted honeycomb lattice* are Na₃Cu₂SbO₆ [24–28], Li₃Cu₂SbO₆ [29, 30], and Na₂Cu₂TeO₆ [26, 28, 31–33]. It should be noted that, despite the similarity in their crystal structures, spin chains in Li₃Cu₂SbO₆ are fragmented due to a considerable site interchange between magnetic Cu²⁺ and non-magnetic Li¹⁺ ions [29, 30, 34, 35]. We further note that a related compound Li₂Cu₂TeO₆ has

* Corresponding author: kittiwit.mat@mahidol.ac.th

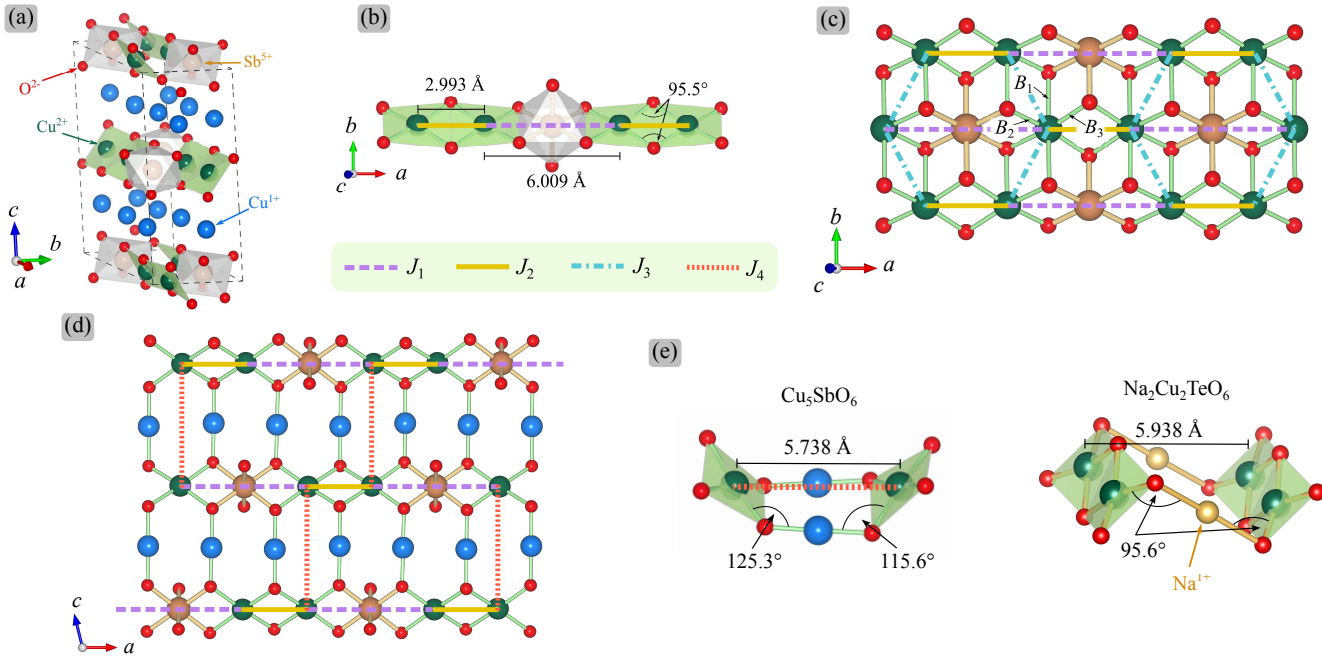


FIG. 1. (a) A monoclinic unit cell of Cu_5SbO_6 is displayed in which spin chains consisted of SbO_6 octahedra (in silver) and edge-sharing Cu_2O_6 double plaquettes (in green) are aligned along the a -axis. The unit cell boundary is indicated by the dashed lines. (b) A chain segment with alternating J_1 and J_2 couplings is shown. The dashed purple and solid yellow lines represent intra-dimer J_1 and inter-dimer J_2 couplings, respectively. (c) The ab -plane projection of a single Cu_2SbO_6 layer is displayed. $B_1 = 2.314$ Å is the Cu-O bond perpendicular to the plaquette whereas $B_2 = 1.994$ Å and $B_3 = 2.043$ Å are the Cu-O bonds within the plaquette. The dot-dash turquoise lines represent inter-chain J_3 couplings. (d) A single layer projected on to the ac -plane is shown, where the dotted orange lines represent inter-chain J_4 couplings perpendicular to the honeycomb planes. The super-exchange path responsible for the J_4 coupling in Cu_5SbO_6 is displayed in (e) along with the corresponding path in $\text{Na}_2\text{Cu}_2\text{TeO}_6$. The crystal structure illustrations are generated by VESTA [23].

also been synthesized [36] but its magnetic characterization still awaits studies. The crystal structure of these compounds can be viewed as a stacking of Na^{1+} layers alternating with Cu_2MO_6 layers where $M = \text{Sb, Te}$ [37–40]. A Cu_2MO_6 layer is built upon edge-sharing elongated CuO_6 octahedra forming a honeycomb lattice of Cu^{2+} ions with M ions positioned at the center of hexagons. The honeycomb lattice is distorted due to a strong Jahn-Teller effect on oxygen octahedra of Cu^{2+} ions. Magnetic characteristics of these archetypal compounds are extensively studied by means of experiments as well as first-principles calculations. Experimental investigations include, for instance, inelastic neutron scattering (INS) [25, 31, 32], ²³Na nuclear magnetic resonance (NMR) [27, 41], and thermodynamics measurements [24, 28, 38, 42, 43]. The experimental studies reveal a finite energy gap with the non-magnetic singlet ground state in these systems. In particular, INS experiments unambiguously show that, at base temperatures, dimers are formed between third-nearest-neighbor rather than first-nearest-neighbor spins. Surprisingly, fitting the energy dispersion of the triplet excitations yields minimal AFM J_3 coupling and FM J_2 coupling that are weaker than AFM J_1 even though the bond length of J_1 is longer than that of J_2 . Here, as indicated in Figs. 1(b) and 1(c),

J_2 and J_3 denote the couplings between the first-nearest-neighbor spins whereas J_1 denotes the coupling between the third-nearest-neighbor spins.

First-principles calculations employing density functional theory (DFT) [26, 28, 33, 38, 42] and density-matrix renormalization group (DMRG) [33] provide a comprehensive microscopic description for such a peculiar behavior of these exchange couplings deduced from experiments. The DFT results suggest that the magnetism of these compounds is primarily governed by the half-filled $\text{Cu}^{2+} 3d_{x^2-y^2}$ orbital, where the local x - and y -axis almost align along $\text{Cu}^{2+}\text{-O}^{2-}$ bonds in the equatorial plane of the octahedron. This explains naturally the subordinate magnitude of J_3 coupling since the $\text{Cu}^{2+}\text{-O}^{2-}\text{-Cu}^{2+}$ path for J_3 incorporates a $\text{Cu}^{2+}\text{-O}^{2-}$ bond (bond B_1 in Fig. 1(c)) that is elongated and perpendicular to the $\text{Cu}^{2+} 3d_{x^2-y^2}$ orbital. That the magnitude of J_1 coupling is much greater than that of J_2 coupling owes to the direct overlap of $\text{Cu}^{2+} 3d_{x^2-y^2}$ orbitals with $\text{O}^{2-} 2p$ orbitals along the $\text{Cu}^{2+}\text{-O}^{2-}\text{-...-O}^{2-}\text{-Cu}^{2+}$ path across the MO_6 octahedron. On the other hand, as displayed in Fig. 1(b), since the angle of the $\text{Cu}^{2+}\text{-O}^{2-}\text{-Cu}^{2+}$ path for J_2 is close to 90°, a pair of $\text{O}^{2-} 2p$ orbitals is almost orthogonal resulting in a weaker J_2 . In accordance with Goodenough-Kanamori-Anderson rules [44–47], the sign

of J_2 coupling is expected to be FM.

Another compound in the family for exploring physics of the quasi-1D alternating dimerized spin chains has been reported in Ref. [48]. The authors of Ref. [48] have synthesized a Delafossite-derived compound Cu_5SbO_6 ($\text{Cu}_3^{1+}\text{Cu}_2^{2+}\text{SbO}_6$) that realizes a distorted honeycomb lattice of Cu^{2+} spins. The crystal structure of Cu_5SbO_6 is built from a monoclinic unit cell, as shown in Fig. 1(a), with the space group $C2/c$ (no. 15) and the lattice parameters $a = 8.923 \text{ \AA}$, $b = 5.593 \text{ \AA}$, $c = 11.845 \text{ \AA}$, and $\beta = 103.585^\circ$. The structure can also be viewed as a stacking of magnetic Cu_2SbO_6 layers alternating with non-magnetic Cu^{1+} layers. According to the measurements performed in Ref. [48], powder sample of Cu_5SbO_6 develops stacking faults which manifest as diffusive streaks along the c^* -axis in a selected-area electron diffraction pattern. The stacking faults can be effectively improved by elevating synthesis temperature. The temperature dependence of magnetic susceptibility and magnetic heat capacity indicates a formation of spin dimers as temperature is lowered below 120 K. An approximated energy gap of ~ 190 K is obtained by fitting susceptibility data with an isolated dimer model. While it is plausible to assume a similar J_1 - J_2 - J_3 magnetic coupling scheme for Cu_5SbO_6 , a DFT calculation [49] suggests a slightly different model. First of all, DFT calculation confirms the alternation of AFM J_1 and FM J_2 as in the case for related compounds. However, it is found that the AFM inter-plane coupling J_4 (see Fig. 1(d)) is significant, and J_3 is even smaller than in the related compounds. By inspecting the crystal structures of Cu_5SbO_6 and $\text{Na}_2\text{Cu}_2\text{TeO}_6$ in between the honeycomb planes, as shown in Fig. 1(e), one can see that the two angles $\text{Cu}^{2+}\text{-O}^{2-}\text{-Cu}^{1+}$ of the super-exchange path $\text{Cu}^{2+}\text{-O}^{2-}\text{-Cu}^{1+}\text{-O}^{2-}\text{-Cu}^{2+}$ in Cu_5SbO_6 amount to about 120° which facilitates the electron exchange more efficiently between the two Cu^{2+} ions compared to $\text{Na}_2\text{Cu}_2\text{TeO}_6$ where the angles $\text{Cu}^{2+}\text{-O}^{2-}\text{-Na}^{1+}$ are close to 90° .

In this article, using neutron spectroscopy and magnetometry we set out to conclude that the J_1 - J_2 - J_4 model is more appropriate for Cu_5SbO_6 . The content of this article is organized as follows. We first present studies of the crystal structure and stacking faults of the compound employing x-ray diffraction, x-ray absorption fine structure, and transmission electron microscopy techniques. Based upon the exchange coupling parameters determined from neutron data, quantum Monte Carlo simulations are performed to compute model temperature-dependent susceptibility and field-dependent magnetization which are, in turn, used to verify with experimental data. Finally, we present an analysis of the powder-averaged inelastic neutron scattering data utilizing a first-order dimer expansion calculation for both J_1 - J_2 - J_3 and J_1 - J_2 - J_4 models.

II. EXPERIMENTAL DETAILS

A. Crystal growth and characterization

Powder samples of Cu_5SbO_6 were prepared by a conventional solid-state reaction from a stoichiometric mixture of CuO and Sb_2O_5 . A homogeneous mixture of the precursors was placed in an alumina crucible and heated in air at 950°C for 24 h followed by an intermediate grinding and re-heating at 1000°C for another 24 h. Single-crystal samples were grown from the obtained powder samples using the vertical-gradient freezing technique. The powder sample with mass ~ 10 g was loaded into a pointed-bottom zirconia crucible and sealed with cement to prevent sample leakage during the growth process. We note that alumina crucibles do not work well with Cu_5SbO_6 due to sample penetration during crystallization from a liquid phase. The sealed crucible placed inside a quartz tube was positioned in a furnace where the temperature was $\sim 1160^\circ\text{C}$ (the melting point) and uniform across the sample inside the crucible. The furnace was set up so that the temperature gradient below the starting point of the crucible was about -10°C/cm . The heating sequence started with increasing the temperature with a rate of 3°C/min from room temperature to 1160°C . After the temperature reaches 1160°C , it was held for 6 h to ensure a complete and homogeneous melting. The sample was then lowered with a rate of 1 cm/day to start the crystallization. The process continued for 4 days before the temperature was decreased down to room temperature with a rate of 3°C/min .

The crystal structure of Cu_5SbO_6 at room temperature was probed with single-crystal and powder x-ray diffraction (XRD) techniques. The former employed a Bruker X8 APEX II CCD Diffractometer with MoK_α radiation, whereas the latter used an Empyrean Diffractometer with CuK_α radiation. A sample for powder diffraction was prepared by thoroughly grinding small pieces of crystals and loosely encased between Mylar C films. The powder XRD was performed in the transmission mode with rotating sample and with $10^\circ \leq 2\theta \leq 80^\circ$. The oxidation states of Cu ions at different crystallographic sites in Cu_5SbO_6 were determined by performing an x-ray absorption fine structure (XAFS) experiment. The experiment was conducted with the multi-x-ray techniques beamline BL1.1W at the Synchrotron Light Research Institute (SLRI) in Thailand. An XAFS spectrum of Cu_5SbO_6 powder at room temperature was obtained at the CuK edge with $8.8 \text{ keV} \leq E \leq 9.8 \text{ keV}$. To determine the edge energy of Cu^{1+} and Cu^{2+} ions, absorption spectra were taken separately from Cu_2O and CuO standards. The amplitude reduction factor of Cu atom was obtained from analyzing a Cu foil spectrum. A characterization of stacking faults was carried out by means of a transmission electron microscope (TEM) with powder samples synthesized at 1000°C and 1150°C . The experiment was performed using a JEOL Electron Microscope equipped with a thermal field-emission electron gun and

an in-column energy filter operating at 100 kV.

B. Magnetometry and neutron spectroscopy

Magnetization of Cu_5SbO_6 in an applied magnetic field oriented parallel (\mathbf{H}_{ab}) and perpendicular (\mathbf{H}_{c^*}) to the honeycomb plane was measured using a Quantum Design MPMS 3 vibrating-sample magnetometer. The temperature dependence was measured from $T = 2$ to 400 K with $H = 100$ Oe whereas the field dependence was measured from $H = 0$ to 7×10^4 Oe at $T = 2$ and 120 K. For both field directions, an aligned crystal sample (see inset of Fig. 2(a)) with mass 9.48 mg was attached to a quartz rod whose magnetization was measured separately under the same conditions.

Magnetic excitations were investigated with inelastic neutron scattering (INS) techniques. INS experiments in zero magnetic field were performed using the cold-neutron time-of-flight (TOF) disk-chopper spectrometer BL14 (AMATERAS) [50] at Japan Proton Accelerator Research Complex and the double-focusing triple-axis (TA) spectrometer BT-7 [51] at NIST Center for Neutron Research. For both spectrometers, due to the unavailability of large single crystals, crystal samples with mosaicity were employed rather than genuine powder samples to effectively avoid stacking-fault issues. Powder averaging for the TOF data was done later using the USTUSEMI software [52]. At AMATERAS, a sample of mass ~ 2 g was loaded in an aluminum can and cooled down to 4 K using a closed cycle ^4He cryostat. The excitation spectra were probed with multiple neutron incident energies including $E_i = 23.7$ meV. The phonon spectrum was measured at 200 K with the same E_i . During the measurement, the sample was rotated around the vertical axis with a step of 1° to cover 172° . At BT-7, the experiment was performed using a sample of mass ~ 1 g with the fixed- E_f mode having a final energy $E_f = 14.7$ meV utilizing pyrolytic graphite monochromator and analyzer. The collimation adopted was open- $80'-80'-120'$ with a single detector providing an energy resolution of 1.5 meV (FWHM) at the elastic position. The temperature was lowered to 2.8 K using a closed cycle ^4He cryostat. The E -scan measurements were taken with a wavevector $Q \sim 2 \text{ \AA}^{-1}$ in a temperature range $2.8 \text{ K} \leq T \leq 200 \text{ K}$, and at $T = 2.8 \text{ K}$ the data were taken in a range $1 \text{ \AA}^{-1} \leq Q \leq 3 \text{ \AA}^{-1}$.

III. RESULTS AND DISCUSSION

A. Crystal structure and stacking faults

Refinements of the crystal structure using the collected single-crystal and powder XRD data are based on the structural model reported in Ref [48]. The refinement with the single-crystal XRD data is performed with 799 unique reflections with $I_{\text{obs}} > 3\sigma$, where I_{obs} and σ are

TABLE I. Optimized atomic parameters of Cu_5SbO_6 obtained from refinements of the single-crystal and powder XRD data taken at room temperature. The unit cell is monoclinic with the space group $C2/c$ (no. 15). The lattice parameters are $a = 8.9291(2)$ Å, $b = 5.5974(1)$ Å, $c = 11.8529(2)$ Å, $\beta = 103.605(1)^\circ$. Numbers in parentheses are one standard deviation.

Atom	Site	x/a	y/b	z/c
Single-crystal x-ray diffraction				
Sb	4c	3/4	3/4	0
Cu(1)	4e	0	0.6243(3)	1/4
Cu(2)	8f	0.8285(1)	0.0968(3)	0.2437(1)
Cu(3)	8f	0.4168(1)	0.7487(2)	0.00175(9)
O(1)	8f	0.4451(8)	0.118(1)	0.0912(6)
O(2)	8f	0.2227(8)	0.924(1)	0.9178(6)
O(3)	8f	0.6176(8)	0.381(1)	0.5969(6)
$R = 6.44\%$, $\text{w}R_2 = 17.7\%$, $\text{GoF} = 2.22$				
Powder x-ray diffraction				
Sb	4c	3/4	3/4	0
Cu(1)	4e	0	0.6251(6)	1/4
Cu(2)	8f	0.8285(4)	0.0969(4)	0.2427(3)
Cu(3)	8f	0.4164(3)	0.749(1)	0.0019(3)
O(1)	8f	0.450(1)	0.112(2)	0.092(1)
O(2)	8f	0.225(1)	0.920(2)	0.916(1)
O(3)	8f	0.615(1)	0.377(2)	0.595(1)
$R_p = 6.42\%$, $R_{wp} = 9.05\%$, $\text{GoF} = 1.87$				

the observed intensity and corresponding standard deviation, respectively, using JANA2020 software package [53]. The refinement result is presented in Fig. 2(a) as a plot of observed structure factor F_{obs} against calculated structure factor F_{cal} computed from the refined atomic parameters listed in Table I. As can be seen in Fig. 2(a), the model provides the values of the calculated structure factor that are fairly consistent with the observed data. The cleavage of a typical crystal was examined with the θ - 2θ scan and was found to be $(00L)$ planes as shown in the inset of Fig. 2(a). Fig. 2(b) displays the powder XRD pattern obtained from ground crystals. Comparing the position of the observed Bragg peaks with that derived from the model (green bars) indicates that impurities in the sample, if present, are negligible. The diffraction pattern is fitted to the model using the Rietveld method [54] as implemented in FULLPROF software suite [55]. The refinement yields the optimized lattice and atomic parameters listed in Table I. The calculated diffraction pattern generated from the so-obtained parameters is illustrated in Fig. 2(b) as a black solid line which fits the observed data fairly well.

While XRD is one of the most powerful techniques for investigating the periodic structure of compounds, it is, however, practically incapable of distinguishing ions that have similar atomic factors as in the case of Cu^{1+} and Cu^{2+} in Cu_5SbO_6 . Namely, while coordinates of

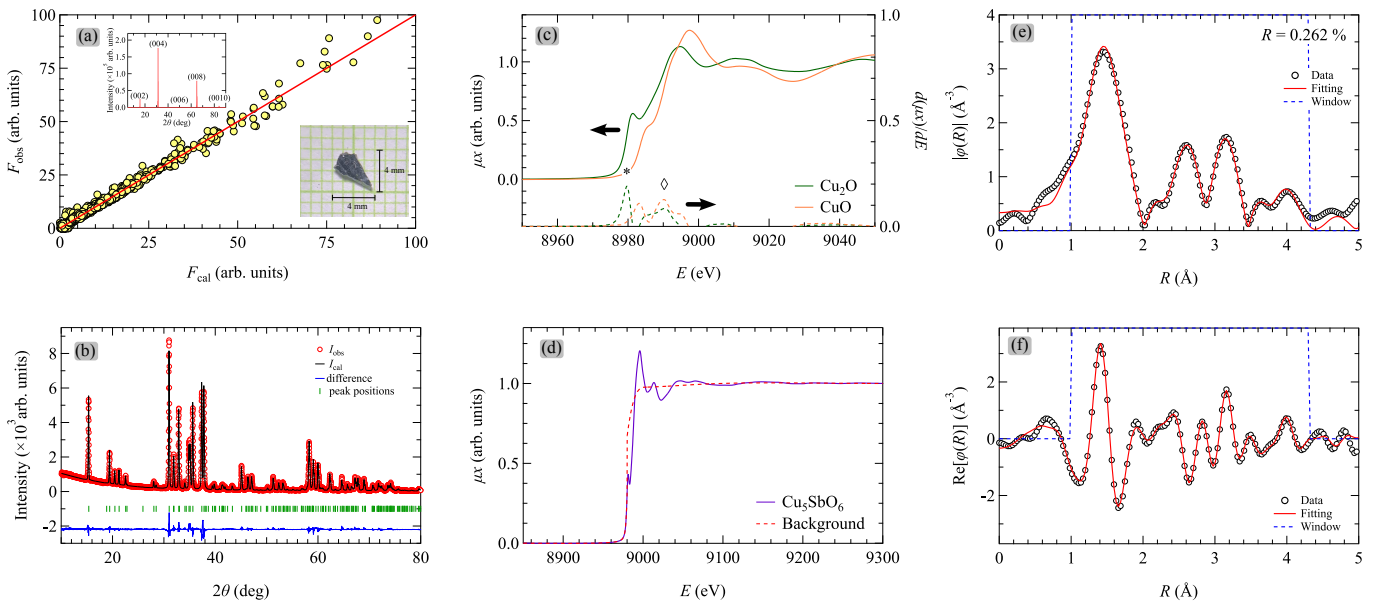


FIG. 2. (a) A plot of F_{obs} against F_{cal} obtained from refinement of the single-crystal XRD data. The straight line is where $F_{\text{obs}} = F_{\text{cal}}$. The insets show a typical single-crystal sample and the θ - 2θ scan of a cleaved facet. (b) Powder XRD pattern of ground crystals. Open circles are observed intensity. The black line represents the calculated intensity based on the refined parameters. The blue line shows the difference between observed and calculated intensities. The green bars mark the position of Bragg peaks. (c) Normalized absorption spectra of CuO (orange) and Cu₂O (green). The absorption coefficient μx is shown on the left axis and the first derivative on the right axis. The asterisk and diamond symbols indicate the edge energy of Cu¹⁺ and Cu²⁺ ions, respectively. (d) Normalized absorption spectrum of Cu₅SbO₆. The dashed line represents background of the spectrum. (e) Modulus of the Fourier transform of $\varphi(k)$ with the real part shown in (f). The open circles represent the data, and the red curve is the fitting with the model described in text. The dotted line is the fitting range (window).

Cu(1), Cu(2) (between honeycomb planes), and Cu(3) (in honeycomb planes) in the unit cell can be accurately identified, their oxidation states must be determined by another method. As Cu¹⁺ and Cu²⁺ are quite similar in size, it is possible to have site interchange between them as in the case of Li₃Cu₂SbO₆ in which considerable amounts of Li¹⁺ and Cu²⁺ ions exchange sites [29, 30]. To confirm that all Cu(3) in Cu₅SbO₆ has 2+ oxidation state and, therefore, form full Cu²⁺ honeycomb layers, we turn to XAFS technique which is more effective for determining the oxidation state of a specific ion. The absorption coefficient, μx , of a material can be obtained from $I = I_0 e^{-\mu x} \Leftrightarrow \mu x = -\ln(I/I_0)$ where I and I_0 are transmitted and incident intensities, respectively. Fig. 2(c) and 2(d) show the collected XAFS spectra of CuO, Cu₂O and Cu₅SbO₆, respectively. Inspection on the results in Fig. 2(c) shows that Cu¹⁺ ions in Cu₂O (green) and Cu²⁺ ions in CuO (orange) have unequal edge energies. Estimated values of edge E_0 for Cu¹⁺ and Cu²⁺ ions are determined from their absorption spectra as the energy E at which the first derivative of μx is maximized, which is done using the ATHENA module in the DEMETER software suite [56]. The first derivatives of $\mu x(E)$ for both Cu₂O and CuO are displayed as dashed lines in Fig. 2(c) with the asterisk and diamond symbols marking the estimated E_0 of Cu¹⁺ and Cu²⁺ ions, respectively. The difference in E_0 of the two ions is about 10 eV.

To determine the oxidation states of Cu ions in

Cu₅SbO₆, we performed the extended x-ray absorption fine structure (EXAFS) analysis. EXAFS analysis is performed in the oscillating region of the spectrum [57] which is quantified by $\varphi(k) \equiv \mu x - \mu_0 x$ where $\mu_0 x$ is the background signal (dashed line in Fig. 2(d)) and k is related to E through $k = \sqrt{2m_e(E - E_0)}/\hbar$. Here m_e is the electron mass. Contrary to XRD that depends upon average periodic structures, EXAFS relies on local environments around a particular ion. As the local environment of Cu sites within the honeycomb planes and that in between the planes are completely different, each site, therefore, produces a distinct oscillating pattern in $\varphi(k)$. To construct a model for the fitting, the crystal structure listed in Table I is used to generate all possible electron scattering paths around each Cu site, and $\varphi(k)$ of Cu₅SbO₆ is then a superposition of $\varphi_i(k)$'s from paths having significant amplitudes. To facilitate the fitting, the observed spectrum is Fourier-transformed to a real-space variable R , whose modulus and real part are illustrated in Figs. 2(e) and 2(f), respectively. The fitting is performed using the ARTEMIS module in the DEMETER software suite [56]. The fitting parameters include path distance corrections δR along with thermal deviations σ , Cu amplitude reduction factor S_0^2 , and edge corrections δE_0 . The amplitude reduction factor S_0^2 for Cu atom is obtained separately from fitting $\varphi(R)$ collected with a Cu foil sample and is found to be 0.89(5). The ini-

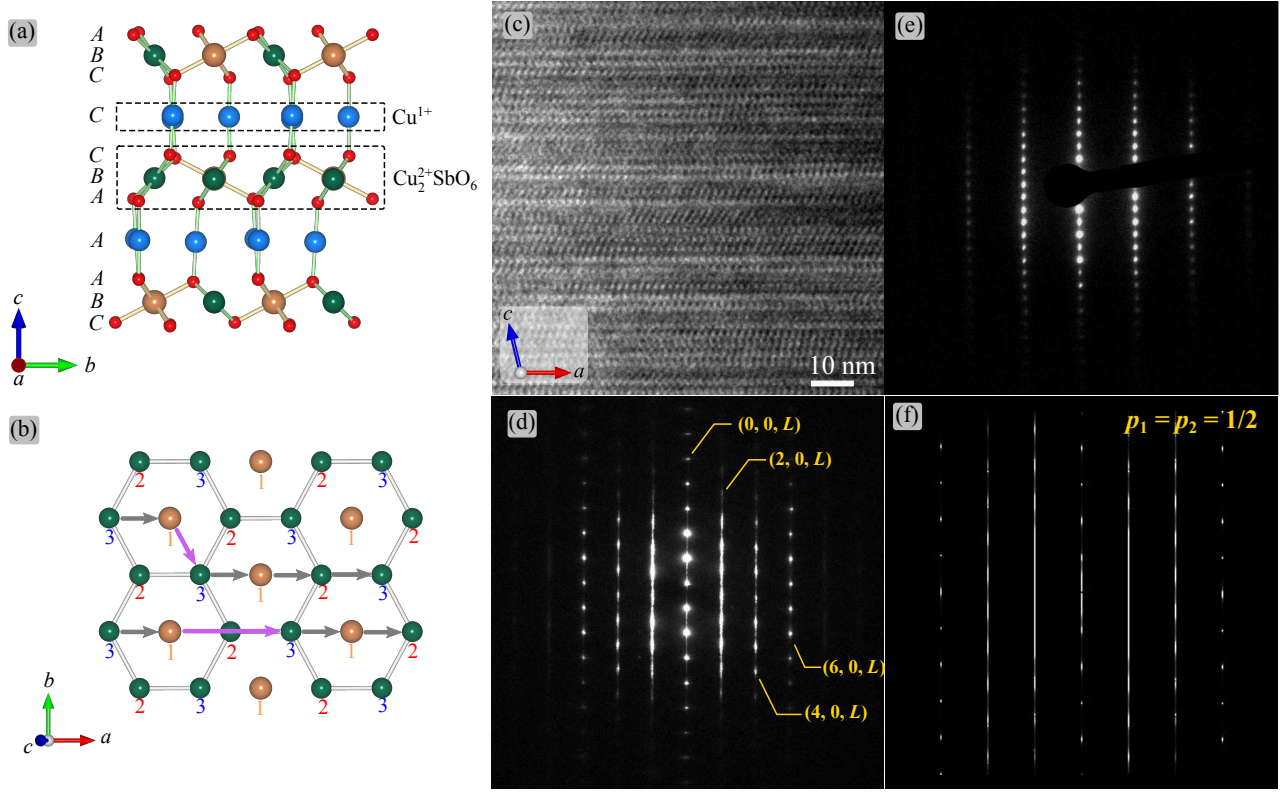


FIG. 3. (a) A projection of the crystal structure onto the bc^* plane showing the ideal stacking sequence of Cu_5SbO_6 . (b) Two equivalent representatives of in-plane translations of a honeycomb layer that contain one stacking fault depicted by the purple arrows. The grey arrows represent the ideal translation vector. ‘1’, ‘2’, and ‘3’ are sub-lattice labels of the honeycomb layer. The atom representations are the same as in Fig. 1(a). (c) A TEM image in the ac plane of the sample synthesized at 1000 °C. (d), (e) SAED patterns in the $(H, 0, L)$ planes of samples synthesized at 1000 °C and 1150 °C, respectively. (f) A simulated SAED pattern computed with $p_1 = p_2 = 1/2$. The crystal structure illustrations are generated by VESTA [23].

tial values of E_0 for each Cu site are set to the value of Cu^{1+} ion, namely, the value marked by the asterisk in Fig. 2(c). The fitting result is shown as red curves in Figs. 2(e) and 2(f) with $R = 0.262\%$. The optimized values of δE_0 for Cu(1) and Cu(2) are found to be the same (and, therefore, are constrained to the same value in the final refinement) which equals to 3.0(5) eV, while δE_0 of Cu(3) is 13.2(3) eV. Hence, E_0 of Cu(3) residing in the honeycomb planes is larger than E_0 of the other two sites in between the planes by about 10 eV, i.e., the oxidation state of Cu(3) is 2+ and that of Cu(1) and Cu(2) is 1+.

As a common feature of several layered compounds, stacking faults, a consequence of multiple in-plane translations that virtually contribute the same amount of energy to the crystal, also occur in Cu_5SbO_6 [48]. A precise description of such a crystallographic defect is crucial as it can potentially affect the magnetic coupling scheme of the compound. To appreciate how stacking faults form in Cu_5SbO_6 , let us first investigate the ideal stacking as depicted in Figs. 3(a) and 3(b), and the stacking fault model is developed by following the strategy discussed in Refs. [58, 59]. A projection of the crystal structure onto the bc^* plane in Fig. 3(a) shows that the ideal stacking

is an alternation of $\text{Cu}_2^{2+}\text{SbO}_6$ slabs and Cu^{1+} layers. A $\text{Cu}_2^{2+}\text{SbO}_6$ slab consists of a Cu^{2+} honeycomb layer with Sb^{5+} at the center of each hexagon enclosed by two O^{2-} layers in the ABC close-pack manner. The alternation results in a recursive $AAABCCCCB$ sequence in which the Cu^{2+} honeycomb layer is located at the B layer. As depicted in Fig. 3(b), a Cu^{2+} honeycomb layer can be decomposed into three sub-lattices denoted by ‘1’, ‘2’, and ‘3’ in which Sb^{5+} ions reside in sub-lattice ‘1’ and Cu^{2+} ions in sub-lattices ‘2’ and ‘3’. Inspecting Fig. 1(d) shows that the ideal stacking corresponds to in-plane translations of Sb^{5+} ions in a recursive ‘123’ sequence as shown in Fig. 3(b) by grey arrows.

A selected-area electron diffraction (SAED) pattern for the powder sample synthesized at 1000 °C is shown in Fig. 3(d) in which diffusive scattering streaks are observed along $(2, 0, L)$ and $(4, 0, L)$ but are absent along $(0, 0, L)$ and $(6, 0, L)$. The streaks observed reflect lack of periodicity in the c^* direction pointing to translations of the Cu^{2+} honeycomb layers that intermittently intervene the ideal ‘123’ sequence. To gain more insight into this mis-translation, we next investigate a TEM image of the ac plane of this sample as displayed in Fig. 3(c). The image clearly features an irregularity in the stacking pat-

tern and hints at the presence of two in-plane translations along the a direction. Inspecting Fig. 3(b) suggests that, in addition to the ideal in-plane translation, there is another possible translation (depicted by purple arrows) of the Cu^{2+} honeycomb layers that translates Sb^{5+} from sub-lattice ‘1’ to ‘3’, ‘3’ to ‘2’, and ‘2’ to ‘1’. Thus, an appropriate model for stacking faults in Cu_5SbO_6 corresponds to intervening the ideal ‘123’ sequence by a stacking-fault translation at certain frequency. It is worth noting that the ideal in-plane translation vector can be represented by $(1/3, 0, 0)$ and that of the stacking fault by $(2/3, 0, 0)$ or, equivalently, $(-1/3, 0, 0)$. This model immediately provides a description for the disappearance of diffusive streaks along $(6, 0, L)$. As the stacking-fault translation vector is $(2/3, 0, 0)$ which can be obtained by adding $(1/3, 0, 0)$ to the ideal translation vector. The additional phase factor caused by the extra $(1/3, 0, 0)$ results in a phase difference of 2π for $(6, 0, L)$ planes, hence, constructive interference. The streaks are not observed along $(0, 0, L)$ since the phase factor due to these planes always adds in-phase irrespectively of the in-plane translations. To further verify the model, a SAED pattern is simulated using FAULTS software package [60–62]. The frequency of the ideal p_1 and of the stacking-fault translations p_2 are introduced which are subjected to a constraint $p_1 + p_2 = 1$. Fig. 3(f) illustrates a simulated SAED pattern of an extreme case where $p_1 = p_2 = 1/2$ which can well reproduce the diffusive intensities along $(2, 0, L)$ and $(4, 0, L)$ in the observed SAED pattern in Fig. 3(d). In addition, the model can also reproduce the broad peak in the XRD data of a powder sample as illustrated in the inset of Fig. 5(a) of Ref. [48].

A SAED pattern for the sample synthesized at 1150 °C, a temperature just below the melting point, shows a strikingly different result as shown in Fig. 3(e). In this case, the diffusive scattering streaks are unobserved reflecting a restoration of the periodicity along the c^* direction. The absence of the diffusive streaks in this SAED pattern is consistent with the absence of peak broadening, especially in $19^\circ < 2\theta < 23^\circ$, in the powder XRD data collected from ground crystals (see Fig. 2(b)). The improvement of stacking faults in Cu_5SbO_6 by raising the synthesis temperature was also reported in Ref. [48].

B. Magnetization

The temperature dependence of magnetic susceptibility, $\chi = M/H$, for the in-plane (\mathbf{H}_{ab}) and out-of-plane (\mathbf{H}_{c^*}) field directions are shown in Fig. 4(a). The holder’s susceptibility measured separately is found to be smaller than the measurement uncertainty of the sample’s susceptibility and is, therefore, neglected. As the temperature decreases from 400 K, a broad peak indicative of short-range correlations develops at 120 K followed by an upturn below 20 K. No signature of thermal phase

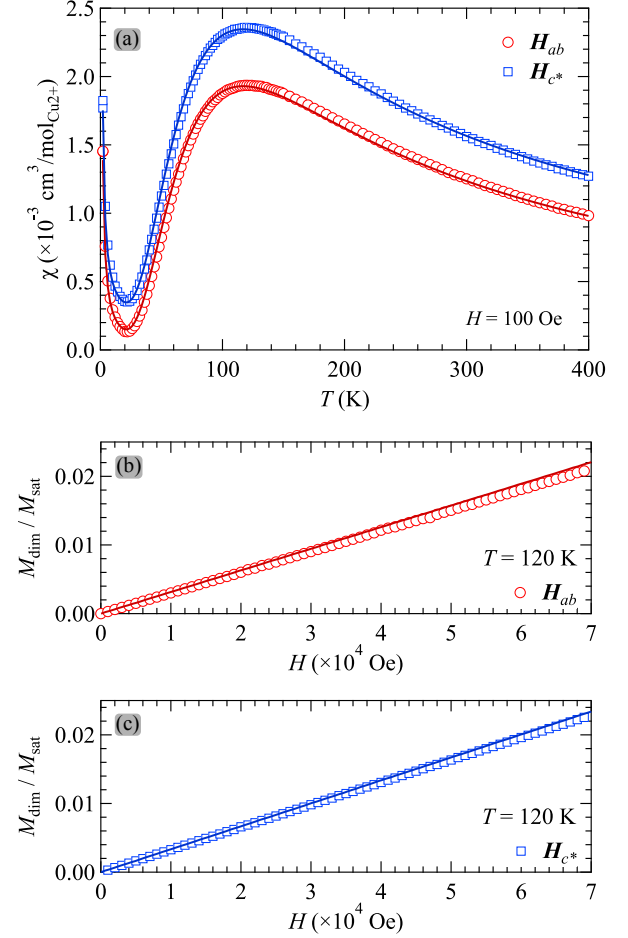


FIG. 4. (a) Magnetic susceptibility as a function of temperature, $\chi(T)$, measured with an applied magnetic field $H = 100 \text{ Oe}$. The solid curves are the best fits. (b), (c) Magnetization of dimerized spins M_{dim} as a function of applied magnetic field normalized with the saturated magnetization $M_{\text{sat}} = \mu_B S$ measured at $T = 120 \text{ K}$. The solid lines are model calculations described in text. The data are collected with \mathbf{H} parallel to the ab plane (circle symbols) and to the c^* axis (square symbols).

transitions is observed down to 2 K. Regardless of the upturn, the absence of anomalies along with the gradual decrease in $\chi(T)$ toward zero suggests the formation of spin dimers in Cu_5SbO_6 at low temperatures. To further investigate the upturn below 20 K, magnetization curves, $M(H)$, for both field directions were measured at 2 K where the signal from dimerized spins can be safely ignored. It is found that the $M(H)$ curves exhibit a Brillouin function that resembles Curie paramagnetism and, therefore, points to the presence of quasi-free spins in the sample under study. Hence, an appropriate model of the susceptibility can be expressed as

$$\chi(T) = f_{\text{free}}\chi_{\text{free}}(T) + f_{\text{dim}}\chi_{\text{dim}}(T) + \chi_0 \quad (1)$$

where f_{free} and f_{dim} are population fractions of quasi-free and dimerized spins, respectively, with a constraint

$\chi_{\text{free}} + f_{\text{dim}} = 1$. χ_0 is a temperature-independent background susceptibility from other non-magnetic ions in Cu₅SbO₆ and core shells of Cu²⁺. $\chi_{\text{free}}(T) = C/T$ with the Curie constant expressed as $C = N_A p^2 \mu_B^2 / (3k_B)$ where N_A is Avogadro constant, μ_B is Bohr magneton, k_B is Boltzmann constant, and $p = g\sqrt{S(S+1)}$ is the effective Bohr magneton number with g being Landé factor of quasi-free spins.

We determine C and f_{free} from the $M(H)$ curves for both field directions measured at $T = 2$ K. To model the $M(H)$ curve at this temperature, two terms responsible for paramagnetic and background magnetization are required. These two terms are $M_{\text{free}}(H) \propto B_{1/2}(H)$ where $B_{1/2}(H)$ is a Brillouin function for $S = \frac{1}{2}$, and $M_0(H) \propto H$. Therefore,

$$M(H) = \frac{1}{2} g\mu_B N_{\text{free}} \tanh\left(\frac{g\mu_B H}{2k_B T}\right) + M_0(H), \quad (2)$$

where $N_{\text{free}} = f_{\text{free}} N_{\text{tot}}$ and N_{free} , N_{tot} are the number of quasi-free and total spins, respectively, in the sample used. By fitting Eq.(2) to the $M(H)$ data at 2 K, we can determine $f_{\text{free}} = 0.00684(6)$ and $C = 0.461(5) \text{ cm}^3 \text{mol}_{\text{Cu}^{2+}}^{-1} \text{K}$ for \mathbf{H}_{c^*} and $f_{\text{free}} = 0.00608(4)$ and $C = 0.457(4) \text{ cm}^3 \text{mol}_{\text{Cu}^{2+}}^{-1} \text{K}$ for \mathbf{H}_{ab} .

We perform quantum Monte Carlo (QMC) simulations to acquire a model for $\chi_{\text{dim}}(T)$. The reduced susceptibility, $\chi^*(t)$, for $0.01 \leq t \leq 10$ where $t = k_B T / J_{\text{max}}$ is calculated using the LOOP algorithm [63, 64] implemented in the ALPS simulation package [65]. The simulation is performed for the J_1 - J_2 - J_4 model with $J_{\text{max}} = J_1 = 16.5$ meV, $J_2 = -6$ meV, and $J_4 = 3$ meV. The determination of these coupling parameters will be discussed in the next section. The simulations are performed on a cluster of 100×100 spins with a periodic boundary condition using 100 000 Monte Carlo steps for thermalization and 500 000 Monte Carlo steps after thermalization. To obtain a functional form of $\chi^*(t)$, we fit simulation results with [66]

$$\chi^*(t) = \frac{\exp(-\Delta^*/t)}{4t} \mathcal{P}_{(r)}^{(q)}(t), \quad (3)$$

where $\mathcal{P}_{(r)}^{(q)}(t)$ is the Padé approximant expressed as

$$\mathcal{P}_{(r)}^{(q)}(t) = \frac{1 + \sum_{n=1}^q N_n / t^n}{1 + \sum_{n=1}^r D_n / t^n}.$$

Here Δ^* , N_n , and D_n are fitting parameters. We have found that the Padé approximant with $q = r = 5$, i.e., $\mathcal{P}_{(5)}^{(5)}(t)$, yields a sufficient accuracy with the deviation between the simulation results and equation (3) in the order of 10^{-3} . $\chi_{\text{dim}}(T)$ is related to $\chi^*(t)$ by

$$\chi_{\text{dim}}(T) = \frac{N_A g^2 \mu_B^2}{J_{\text{max}}} \chi^* \left(\frac{k_B T}{J_{\text{max}}} \right). \quad (4)$$

We fit the experimental data with Eq. (1) where $\chi_{\text{dim}}(T)$ is given by Eq. (4) to extract the Landé factor g and

χ_0 for each field direction. The best fits are shown as solid curves in Fig. 4(a), and the optimized parameters are $g_{ab} = 2.177(2)$, $\chi_0 = 0 \text{ cm}^3 \text{mol}_{\text{Cu}^{2+}}^{-1}$ and $g_{c^*} = 2.309(2)$, $\chi_0 = 1.78(2) \times 10^{-4} \text{ cm}^3 \text{mol}_{\text{Cu}^{2+}}^{-1}$ for \mathbf{H}_{ab} and \mathbf{H}_{c^*} , respectively.

To reaffirm the optimized parameters, we further perform quantum Monte Carlo (QMC) simulations to calculate the reduced magnetization, $M^*(h)$, with the same set of coupling parameters for $0 \leq h \leq 7 \times 10^{-2}$ where $h = g\mu_B H / J_{\text{max}}$ and $T = 120$ K using the DIRECTED-LOOP [67, 68] algorithm. The calculation conditions are the same as for $\chi^*(t)$. $M_{\text{dim}}(H)$ is related to $M^*(h)$ by

$$M_{\text{dim}}(H) = g\mu_B M^* \left(\frac{g\mu_B H}{J_{\text{max}}} \right).$$

The simulated $M_{\text{dim}}(H)$ is calculated with the optimized Landé factor g and then compared with the background-corrected experimental data. As seen in Figs. 4(b) and 4(c), a reasonable agreement is achieved between the data and model calculations confirming the validity of the Landé factors and the exchange couplings.

C. Triplet excitations

Data reduction and powder averaging of the TOF INS data collected from the AMATERAS spectrometer were performed using the UTSUSEMI software package [52]. The obtained intensity maps at $T = 4$ K and 200 K are displayed in Figs. S.1(a) and S.1(b), respectively, in the Supplemental Information (SI). Also included in Fig. S.1(a) is the excitation energy (circle symbols) extracted from the E -scan data taken from the BT-7 spectrometer at $T = 2.8$ K. In Fig. S.1(b), at $T = 200$ K where the magnetic correlations are expected to subside (see also Fig. 6(a)), there remain excitations whose intensity noticeably increases with the magnitude of the wavevector Q and temperature. We, therefore, attribute these excitations to phonons. To obtain the magnetic scattering intensity map, $I_{\text{mag}}(Q, \omega)$, as shown in Fig. 5(a), we subtracted the data at the two temperatures after rescaling the data at 200 K by the temperature-dependent factor $1 + n(T) = (1 - \exp(-E/k_B T))^{-1}$ where $n(T)$ is the Bose factor. It should be noted that the scattering intensity seen at $\hbar\omega = 12$ meV and $Q > 3 \text{ \AA}^{-1}$ is most likely due to residual phonon intensity. To acquire the key characteristics of the magnetic scattering, $I_{\text{mag}}(Q, \omega)$ is then integrated over the wavevector $1 \text{ \AA}^{-1} \leq Q \leq 3 \text{ \AA}^{-1}$. The integrated intensity shown in Fig. S.2(b) features two peaks at $\hbar\omega = 15$ meV and 18 meV and covers an extensive range from the band bottom at ~ 11 meV to the band top at ~ 21 meV amounting to a sizable bandwidth of ~ 10 meV. No magnetic excitation is detected at $\hbar\omega \lesssim 11$ meV or $\hbar\omega \gtrsim 21$ meV.

To explore the temperature evolution of the excitation spectrum, we next examine the TA E -scan data collected at base and elevated temperatures from the

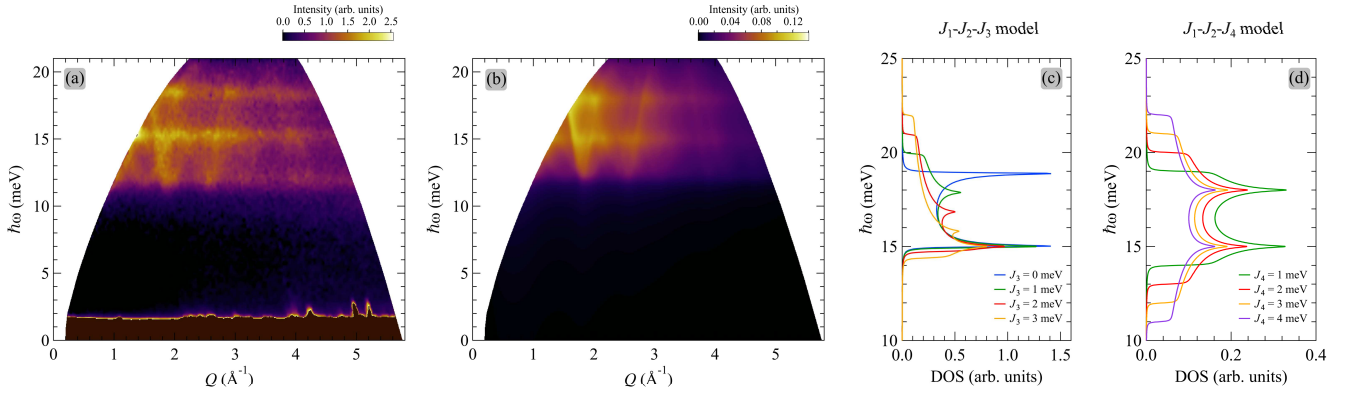


FIG. 5. (a) The observed powder-averaged magnetic intensity map at $T = 4$ K (b) The calculated powder-averaged magnetic intensity map using the J_1 - J_2 - J_4 model with $J_1 = 16.5$ meV, $J_2 = -6$ meV, and $J_4 = 3$ meV. (c) The density of states (DOS) of the J_1 - J_2 - J_3 model and of (d) the J_1 - J_2 - J_4 model.

BT-7 spectrometer. Fig. 6(a) shows the data measured at $2.8 \text{ K} \leq T \leq 200 \text{ K}$ with a fixed wavevector $Q = 1.96 \text{ \AA}^{-1}$. At $T = 2.8 \text{ K}$, the data exhibit three excitation peaks at 12 meV, 15 meV, and 18 meV, denoted by P , M_1 , and M_2 , respectively. At elevated temperatures, the P peak becomes stronger whereas the M_1 and M_2 peaks weaken and eventually disappear at 200 K. Therefore, the M_1 and M_2 peaks are consistent with the two peaks observed in the integrated magnetic intensity shown in Fig. S.2(b). For the P peak, however, it is essential to note that in the TOF data (see Figs. S.1(a) and S.1(b) in the SI) there exist a phonon band as well as magnetic scattering at $\hbar\omega = 12$ meV. Therefore, the P peak, especially at $T = 2.8 \text{ K}$, results from the superposition of these two sources. As the temperature is elevated, the magnetic contribution diminishes leaving only the enhanced phonon contribution. We fit the spectra to a Lorentzian function combined with a linear background to acquire the excitation energy, $\hbar\omega$, for each T and Q . The width of the M_1 and M_2 peaks are assumed identical. Fitting the data (i) at $T = 2.8 \text{ K}$ and with $1.12 \text{ \AA}^{-1} \leq Q \leq 3.09 \text{ \AA}^{-1}$ and (ii) at $2.8 \text{ K} \leq T \leq 200 \text{ K}$ with $Q = 1.96 \text{ \AA}^{-1}$ yields $\hbar\omega$ plotted as circle symbols in Fig. S.1(a) and a T -dependent $\hbar\omega$ shown in Fig. 6(b). In alignment with $\chi(T)$ data, the monotonic increase in $\hbar\omega(T)$ points out that the gapped excitation observed in Cu_5SbO_6 is a triplet excitation (or triplon) since, in a dimerized magnet, triplons are subjected to the hardcore constraint that prevents them from occupying the same dimer site resulting in repulsion between them [69–72] as opposed to long-range ordered magnets for which the gap decreases with increasing temperature due to the reduction in ordered moment.

To acquire an appropriate spin Hamiltonian for Cu_5SbO_6 , we employ the first-order dimer expansion to derive the energy dispersion, ΔE_Q , of triplet excitations for both J_1 - J_2 - J_3 and J_1 - J_2 - J_4 models (a detailed derivation can be found in the Appendix). The expressions for

the dispersion of both models are given in Eqs. (A.10) and (A.11). In these expressions, the wavevector Q is written in terms of the basis vectors \mathbf{b}_1 , \mathbf{b}_2 , and \mathbf{b}_3 defined in Eqs. (A.4)-(A.6). Here, q_i represents the component of each basis vector. Let us begin with the J_1 - J_2 - J_3 model with the dispersion given in Eq. (A.10). For an isolated FM-AFM chain, the dispersion along the q_1 direction oscillates around the energy set by the intra-dimer AFM J_1 coupling with the amplitude determined by the magnitude of the inter-dimer FM J_2 coupling. The incorporation of the interchain AFM J_3 coupling predominantly only results in a modulation of the top of the dispersion along the q_2 direction (see Figs. 8(a)-8(d)). To see how the dispersion produces the M_1 and M_2 peaks in the magnetic scattering, we consider the density of states (DOS), $D(\omega)$, as defined by

$$D(\omega) \propto \int d\mathbf{Q} \delta(\hbar\omega - \Delta E_Q),$$

where the integration is over a unit cell of the reciprocal lattice formed by dimers. Approximating the delta function by a Lorentzian function, $\delta(x) = \epsilon/\pi(x^2 + \epsilon^2)$, where ϵ is a small positive number, we finally obtain DOS for the J_1 - J_2 - J_3 model as shown in Fig. 5(c). The result is presented for four different values of the interchain coupling J_3 with $J_1 = 16.95$ meV, $J_2 = -3.9$ meV. When $J_3 = 0$, two peaks appear at the top and bottom of the DOS. As J_3 increases, the peak at the top shifts towards lower energy and the tail develops towards higher energy. Although $J_3 \approx 1$ meV correctly reproduces peaks in DOS at 15 meV and 18 meV, this model does not provide a tail below 15 meV regardless of the value of J_3 which is in contradiction to the observed spectrum. Therefore, the J_1 - J_2 - J_3 model is not viable in explaining the data.

We next turn to the J_1 - J_2 - J_4 model. The introduction of the interlayer AFM J_4 coupling to the system of isolated FM-AFM chains delivers a slightly distinct effect on the dispersion. Unlike with J_3 , it is found that modulation along the q_3 direction appears at both the top and the

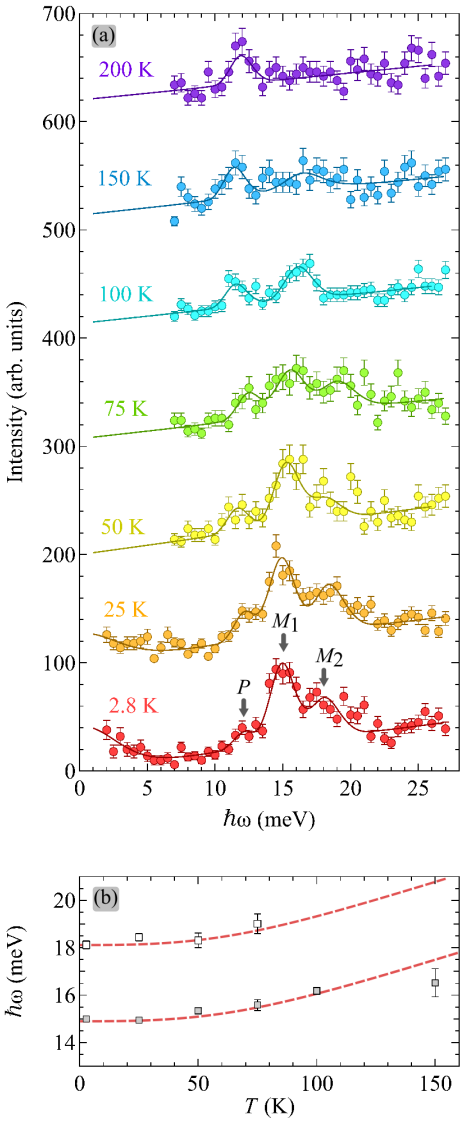


FIG. 6. (a) E -scan data with $Q = 1.97 \text{ \AA}^{-1}$ at 2.8 K. Solid lines are best fits to the model described in text. (b) Temperature dependence of $\hbar\omega$ for M_1 (solid squares) and M_2 (open squares) peaks. Dashed lines are guides to the eyes. Error bars represent one standard deviation.

bottom of the dispersion (see Figs. 8(e)-8(h)). To obtain DOS for this model, we first consider the dispersion in Eq. (A.11) from which the energy of M_1 and M_2 peaks, denoted by E_1 and E_2 , respectively, are given by

$$E_1 = J_1 - \frac{|J_2|}{2} + \frac{|J_4|}{2},$$

$$E_2 = J_1 + \frac{|J_2|}{2} - \frac{|J_4|}{2},$$

which give $2J_1 = E_1 + E_2$ and $|J_2| = |J_4| + (E_2 - E_1)$. Using $E_1 = 15.0(1)$ meV and $E_2 = 18.0(2)$ meV, we can identify $J_1 = 16.5(1)$ meV and $|J_2| = |J_4| + 3.0$ meV. Fig. 5(d) shows DOS of the J_1 - J_2 - J_4 model calculated with

four different values of $|J_4|$. With these coupling parameters the DOS correctly reproduces peaks at 15 meV and 18 meV. Moreover, in contrast to the previous model, as J_4 increases, tails in DOS develop at both higher and lower energy which resembles the pattern observed in the INS spectrum. Based on the INS data, one can obtain an estimate of $|J_4| \approx 3$ meV, and, thus, $|J_2| \approx 6$ meV. It is essential to note that in the presence of stacking faults, although the magnitude of J_4 might be unchanged as the path responsible for the coupling still involves the same ions and geometry, the dimer connectivity is different and the J_1 - J_2 - J_4 model might be inapplicable.

It is natural to extend the model to include the J_3 coupling in the J_1 - J_2 - J_4 model. To this end, let us examine the effect of J_3 on the current model by calculating the DOS of the extended model with different values of J_3 as described in the SI. As can be seen in Fig. S.2(c), the presence of the J_3 coupling results in a suppression of the 18 meV peak and a further elongation of the tail above 21 meV. These effects become more enhanced as J_3 grows. Comparison with the integrated magnetic intensity in Fig. S.2(b) suggests an upper bound for J_3 of merely ~ 0.3 meV, which can safely be neglected when taking the uncertainty of the coupling parameters into account. Finally, to verify the J_1 - J_2 - J_4 model, a powder-averaged INS spectrum was simulated using the proposed set of coupling parameters as outlined in the SI. The simulated result shown in Fig. 5(b) compares very well with the observed spectrum justifying the J_1 - J_2 - J_4 model as adequate and appropriate for Cu_5SbO_6 .

Future INS studies on high-quality single-crystal samples may shed more light on some exotic aspects of the triplon excitations and allow the spin-spin correlations to be mapped out more precisely. The latter, as discussed in Refs. [73–75], play a crucial role in determining the degree of hidden quantum entanglement in a many-body system such as a spin chain. It has been argued in these studies that the spatial extent of quantum entanglement is directly related to the spin-spin correlations that can be measured experimentally by means of the neutron scattering technique. In this arena, as pointed out in Ref. [22], an alternating FM-AFM Heisenberg spin chain may triumph over its alternating AFM-AFM counterpart owing to the non-zero spin-spin correlations on both FM and AFM bonds. Given this, Cu_5SbO_6 can serve as a model system for exploring the spatial evolution of quantum entanglement manifesting in a many-body system.

IV. CONCLUSION

We employed x-ray spectroscopy and electron microscopy to refine the crystal structure and the stacking fault model of Cu_5SbO_6 . Based on the crystal structure, Cu_5SbO_6 can accommodate alternating FM-AFM dimerized spin chains similar to the related compounds with the FM bond forming between Cu^{2+} ions within the Cu_2O_6 double plaquettes and the AFM bond, hence, the

dimers, forming across the hexagon in the honeycomb planes. However, in contrast to the related compounds, the inter-chain couplings that arise between the honeycomb planes can be significant for Cu_5SbO_6 owing to the different geometry of the super-exchange paths that enhance orbital overlap. Stacking faults present in powder samples are a result of two inequivalent in-plane translations, i.e., $(1/3, 0, 0)$ and $(2/3, 0, 0)$, that interchangeably shift the honeycomb planes along the a -direction with a frequency depending on the synthesis temperature.

Based on a first-order dimer expansion approximation, we showed that, unlike the related compounds, the J_1 - J_2 - J_3 model cannot be a complete description for the magnetic properties of Cu_5SbO_6 . With a specific set of coupling parameters, the density of states of such a model, whereas containing peaks at 15 meV and 18 meV, does not exhibit a tail below 15 meV in the INS spectrum. On the other hand, the J_1 - J_2 - J_4 model is capable of reproducing the entire spectrum and, therefore, proves to be a more appropriate starting point for the spin Hamiltonian for Cu_5SbO_6 . The coupling parameters of the J_1 - J_2 - J_4 model estimated from the powder-averaged INS data are $J_1 = 16.5(1)$ meV, $|J_2| \approx 6$ meV, and $|J_4| \approx 3$ meV. With the obtained coupling parameters, we further tested the model by simulating a temperature-dependent susceptibility and field-dependent magnetization. Fitting the simulated susceptibility to the experimental data returns sensible Landé factors, i.e., $g_{ab} = 2.177(2)$ and $g_{c^*} = 2.309(2)$, for Cu^{2+} moments in plaquette environments. Moreover, the simulated magnetization curves calculated with the optimized Landé factors compare reasonably well with the experimental data. Considering these results, Cu_5SbO_6 may be included in a rare collection of compounds that host interacting FM-AFM quantum spin chains which can serve as a playground for exploring novel emergent quantum collective phenomena.

ACKNOWLEDGMENTS

This research has received funding support from the NSRF via the Program Management Unit for Human Resources & Institutional Development, Research and Innovation (PMU-B) (Grant No. B13F680079). Work at Mahidol University was partly supported by the Thailand Center of Excellence in Physics and Mahidol University (Strategic Research Fund): fiscal year 2024. C.P. is grateful for the support by the DPST scholarship from the Institute for the Promotion of Teaching Science and Technology. C.P. and K. Matan thank Dr. Khetpakorn Chakarawet from the Department of Chemistry, Mahidol University, for his assistance in single-crystal XRD measurements. C.P. and K. Matan thank Masaki Ageishi for his assistance in TEM experiments at Tohoku University, Japan. W.-T.C. acknowledges the support of the National Science and Technology Council in Taiwan (Grants No. 113-2124-M-002-006 and 114-2124-M-002-010) and the Featured Research Center Program within the frame-

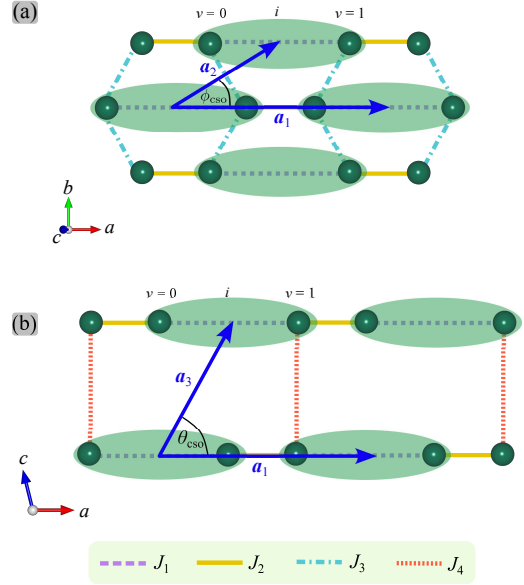


FIG. 7. A lattice formed by dimers depicted as green ovals for the J_1 - J_2 - J_3 and J_1 - J_2 - J_4 models are shown in (a) and (b), respectively. i is the dimer identifier in the lattice, and $\nu = 0, 1$ is the spin identifier in the dimer. \mathbf{a}_1 , \mathbf{a}_2 , and \mathbf{a}_3 are the primitive translation vectors.

work of the Higher Education Sprout Project by the Ministry of Education in Taiwan (Grants No. 113L9008). K. Morita was supported by JSPS KAKENHI (Grant No. JP25K07230). The experiment on AMATERAS was performed with the approval of J-PARC (Proposal No. 2019A0194 (R)). We are grateful for the support from the National Institute of Standards and Technology, U.S. Department of Commerce, for providing neutron research facilities used in this work. The identification of any commercial product or trade name does not imply endorsement or recommendation by the National Institute of Standards and Technology. Synchrotron Light Research Institute (Public Organization), Thailand, is acknowledged for the provision of XAS beamtime.

Appendix: Dimer expansion for triplet excitations

In this appendix, the dispersion relation as well as the dynamical structure factor for the J_1 - J_2 - J_3 and J_1 - J_2 - J_4 models are derived. Fig. 7 shows the lattices formed by dimers for the two models where the primitive translation vectors \mathbf{a}_1 , \mathbf{a}_2 , \mathbf{a}_3 are expressed as

$$\mathbf{a}_1 = l_1 \mathbf{e}_x, \quad (A.1)$$

$$\mathbf{a}_2 = l_2 (\cos \phi_{\text{cso}} \mathbf{e}_x + \sin \phi_{\text{cso}} \mathbf{e}_y), \quad (A.2)$$

$$\mathbf{a}_3 = l_3 (\cos \theta_{\text{cso}} \mathbf{e}_x + \sin \theta_{\text{cso}} \mathbf{e}_z). \quad (A.3)$$

\mathbf{a}_1 and \mathbf{a}_2 form the dimer lattice of the J_1 - J_2 - J_3 model whereas \mathbf{a}_1 and \mathbf{a}_3 form that of the J_1 - J_2 - J_4 model. The primitive translation vectors of the reciprocal dimer lat-

tice \mathbf{b}_1 , \mathbf{b}_2 , \mathbf{b}_3 are

$$\mathbf{b}_1 = \frac{2\pi}{l_1} (\mathbf{e}_x - \cot \phi_{\text{cso}} \mathbf{e}_y - \cot \theta_{\text{cso}} \mathbf{e}_z), \quad (\text{A.4})$$

$$\mathbf{b}_2 = \frac{2\pi}{l_2} \csc \phi_{\text{cso}} \mathbf{e}_y, \quad (\text{A.5})$$

$$\mathbf{b}_3 = \frac{2\pi}{l_3} \csc \theta_{\text{cso}} \mathbf{e}_z. \quad (\text{A.6})$$

\mathbf{b}_1 and \mathbf{b}_2 form the reciprocal dimer lattice of the J_1 - J_2 - J_3 model whereas \mathbf{b}_1 and \mathbf{b}_3 form that of the J_1 - J_2 - J_4 model. Note that for Cu_5SbO_6 , $l_1 = 9.00 \text{ \AA}$, $l_2 = 5.30 \text{ \AA}$, $l_3 = 6.55 \text{ \AA}$, $\theta_{\text{cso}} = 62^\circ$, $\phi_{\text{cso}} = 30^\circ$.

1. Energy dispersion

In our Hamiltonian $H = H_0 + H'$ for the two models, the common unperturbed term H_0 is defined by

$$H_0 = J_1 \sum_i \mathbf{S}_{i,0} \cdot \mathbf{S}_{i,1},$$

where i is an identifier given to a dimer and $\mathbf{S}_{i,\nu}$ is the ν -th spin operator on the i -th dimer (see Fig. 7). The perturbation term H' for each model is given by

$$\begin{aligned} H'_{123} &= J_2 \sum_i \mathbf{S}_{i,1} \cdot \mathbf{S}_{i+\mathbf{a}_1,0} \\ &\quad + J_3 \sum_i \mathbf{S}_{i,1} \cdot (\mathbf{S}_{i+\mathbf{a}_2,0} + \mathbf{S}_{i+\mathbf{a}_1-\mathbf{a}_2,0}), \\ &= \sum_i \sum_{\rho=\mathbf{a}_1, \mathbf{a}_2, \mathbf{a}_1-\mathbf{a}_2} J_\rho \mathbf{S}_{i,1} \cdot \mathbf{S}_{i+\rho,0} \\ H'_{124} &= J_2 \sum_i \mathbf{S}_{i,1} \cdot \mathbf{S}_{i+\mathbf{a}_1,0} \\ &\quad + J_4 \sum_i \mathbf{S}_{i,1} \cdot \mathbf{S}_{i+\mathbf{a}_1-\mathbf{a}_3,0}, \\ &= \sum_i \sum_{\rho=\mathbf{a}_1, \mathbf{a}_1-\mathbf{a}_3} J_\rho \mathbf{S}_{i,1} \cdot \mathbf{S}_{i+\rho,0}. \end{aligned}$$

The wave function of the singlet sea $|s\rangle$ is expressed as

$$|s\rangle = \prod_n |s\rangle_n, \text{ where } |s\rangle_n \equiv \frac{1}{\sqrt{2}} (|\uparrow\downarrow\rangle_n - |\downarrow\uparrow\rangle_n).$$

Here $|\uparrow\downarrow\rangle_n$, $|\downarrow\uparrow\rangle_n$, ... represent the state of the n -th dimer in the Ising basis. We also define the single-triplet-dimer state $|t_l^+\rangle$ (STD), in which only the l -th dimer in the singlet sea is in $|t^+\rangle_l \equiv |\uparrow\uparrow\rangle_l$, as

$$|t_l^+\rangle = |t^+\rangle_l \prod_{n(\neq l)} |s\rangle_n.$$

Multiplying H_0 by $|t_l^+\rangle$, we immediately get

$$H_0 |t_l^+\rangle = J_1 \sum_i (\mathbf{S}_{i,0} \cdot \mathbf{S}_{i,1}) |t_l^+\rangle = J_1 \left(-\frac{3}{4} N + 1 \right) |t_l^+\rangle.$$

Next, we multiply H' by $|t_l^+\rangle$. Notice that each exchange operator in the perturbation term involves two dimers. In order to evaluate $H' |t_l^+\rangle$, we explicitly calculate the following three patterns of terms for the two dimers. The first one is $\mathbf{S}_{l,1} \cdot \mathbf{S}_{l+\rho,0} |t^+\rangle_l |s\rangle_{l+\rho}$, which can be evaluated as

$$\begin{aligned} \mathbf{S}_{l,1} \cdot \mathbf{S}_{l+\rho,0} |t^+\rangle_l |s\rangle_{l+\rho} &= \left[S_{l,1}^z S_{l+\rho,0}^z + \frac{1}{2} \left(\underbrace{S_{l,1}^+ S_{l+\rho,0}^-}_{\rightarrow 0} + S_{l,1}^- S_{l+\rho,0}^+ \right) \right] |t^+\rangle_l |s\rangle_{l+\rho} \\ &= \frac{1}{4} |t^+\rangle_l |t^0\rangle_{l+\rho} - \frac{1}{2} \frac{1}{\sqrt{2}} (|t^0\rangle_l + |s\rangle_l) \frac{1}{\sqrt{2}} |t^+\rangle_{l+\rho} \\ &= -\frac{1}{4} |s\rangle_l |t^+\rangle_{l+\rho} + \frac{1}{4} |t^+\rangle_l |t^0\rangle_{l+\rho} - \frac{1}{4} |t^0\rangle_l |t^+\rangle_{l+\rho}, \end{aligned}$$

which gives

$$\mathbf{S}_{l,1} \cdot \mathbf{S}_{l+\rho,0} |t_l^+\rangle = -\frac{1}{4} |t_{l+\rho}^+\rangle + (\text{non-STD states}).$$

The second one is $\mathbf{S}_{l-\rho,1} \cdot \mathbf{S}_{l,0} |s\rangle_{l-\rho} |t^+\rangle_l$, which can be

evaluated as

$$\begin{aligned} \mathbf{S}_{l-\rho,1} \cdot \mathbf{S}_{l,0} |s\rangle_{l-\rho} |t^+\rangle_l &= -\frac{1}{4} |t^+\rangle_{l-\rho} |s\rangle_l - \frac{1}{4} |t^0\rangle_{l-\rho} |t^+\rangle_l \\ &\quad + \frac{1}{4} |t^+\rangle_{l-\rho} |t^0\rangle_l, \end{aligned}$$

which gives

$$\mathbf{S}_{l-\rho,1} \cdot \mathbf{S}_{l,0} |t^+\rangle = -\frac{1}{4} |t^+\rangle_{l-\rho} + (\text{non-STD states}).$$

The final one is $\mathbf{S}_{i,1} \cdot \mathbf{S}_{i+\rho,0} |s\rangle_i |s\rangle_{i+\rho}$ with $i \neq l$ and $i + \rho \neq l$, which can be evaluated as

$$\begin{aligned} \mathbf{S}_{i,1} \cdot \mathbf{S}_{i+\rho,0} |s\rangle_i |s\rangle_{i+\rho} &= -\frac{1}{4} |t^0\rangle_i |t^0\rangle_{i+\rho} + \frac{1}{4} |t^+\rangle_i |t^-\rangle_{i+\rho} \\ &\quad - \frac{1}{4} |t^-\rangle_i |t^+\rangle_{i+\rho}, \end{aligned}$$

which gives

$$\mathbf{S}_{i,1} \cdot \mathbf{S}_{i+\rho,0} |t^+\rangle = (\text{non-STD states}).$$

Using the above results, $H' |t_l^+\rangle$ can be evaluated as follows:

$$H' |t_l^+\rangle = -\frac{1}{4} \sum_{\rho} J_{\rho} (|t_{l+\rho}^+\rangle + |t_{l-\rho}^+\rangle) + (\text{non-STD states}).$$

Let H_{eff} be the effective Hamiltonian of the STD states, in which the energy is measured from the ground-state energy

$$E_g = -\frac{3}{4} J_1 N + (\text{second-order or higher terms}).$$

Then, the matrix elements of H_{eff} within the first-order perturbation for each model are found to be

$$\begin{aligned} \langle t_{l'}^+ | H_{\text{eff}}^{123} | t_l^+ \rangle &\simeq \langle t_{l'}^+ | H_0 | t_l^+ \rangle + \langle t_{l'}^+ | H'_{123} | t_l^+ \rangle - E_g \delta_{l',l} \\ &= J_1 \delta_{l',l} - \frac{1}{4} \sum_{\rho} J_{\rho} (\delta_{l',l+\rho} + \delta_{l',l-\rho}) \\ &= J_1 \delta_{l',l} - \frac{J_2}{4} (\delta_{l',l+\mathbf{a}_1} + \delta_{l',l-\mathbf{a}_1}) \\ &\quad - \frac{J_3}{4} (\delta_{l',l+\mathbf{a}_2} + \delta_{l',l-\mathbf{a}_2} + \delta_{l',l+\mathbf{a}_1-\mathbf{a}_2} + \delta_{l',l-\mathbf{a}_1+\mathbf{a}_2}), \\ \langle t_{l'}^+ | H_{\text{eff}}^{124} | t_l^+ \rangle &\simeq \langle t_{l'}^+ | H_0 | t_l^+ \rangle + \langle t_{l'}^+ | H'_{124} | t_l^+ \rangle - E_g \delta_{l',l} \\ &= J_1 \delta_{l',l} - \frac{1}{4} \sum_{\rho} J_{\rho} (\delta_{l',l+\rho} + \delta_{l',l-\rho}) \\ &= J_1 \delta_{l',l} - \frac{J_2}{4} (\delta_{l',l+\mathbf{a}_1} + \delta_{l',l-\mathbf{a}_1}) \\ &\quad - \frac{J_4}{4} (\delta_{l',l+\mathbf{a}_1-\mathbf{a}_3} + \delta_{l',l-\mathbf{a}_1+\mathbf{a}_3}). \end{aligned}$$

To diagonalize H_{eff} , we introduce a Fourier transform:

$$|t_{\mathbf{Q}}^+\rangle = \frac{1}{\sqrt{N}} \sum_i |t_i^+\rangle e^{-i\mathbf{Q} \cdot \mathbf{r}_i},$$

where N is the total number of dimers, and \mathbf{r}_i is the position vector of the i -th dimer. This transformation diagonalizes the effective Hamiltonian and gives the triplet excitation spectrum $\Delta E_{\mathbf{Q}} \equiv \langle t_{\mathbf{Q}}^+ | H_{\text{eff}} | t_{\mathbf{Q}}^+ \rangle$:

$$\begin{aligned} \Delta E_{\mathbf{Q}}^{123} &= J_1 - \frac{J_2}{2} \cos(\mathbf{Q} \cdot \mathbf{a}_1) \\ &\quad - J_3 \cos\left(\frac{\mathbf{Q} \cdot \mathbf{a}_1}{2}\right) \cos\left[\mathbf{Q} \cdot \left(\mathbf{a}_2 - \frac{1}{2}\mathbf{a}_1\right)\right]. \end{aligned} \quad (\text{A.7})$$

Similarly, for the J_1 - J_2 - J_4 model,

$$\Delta E_{\mathbf{Q}}^{124} = J_1 - \frac{J_2}{2} \cos(\mathbf{Q} \cdot \mathbf{a}_1) - \frac{J_4}{2} \cos[\mathbf{Q} \cdot (\mathbf{a}_3 - \mathbf{a}_1)]. \quad (\text{A.8})$$

Defining $\mathbf{Q} = q_1 \mathbf{b}_1 + q_2 \mathbf{b}_2 + q_3 \mathbf{b}_3$, we then have

$$\mathbf{Q} \cdot \mathbf{a}_j = \sum_i q_i (\mathbf{b}_i \cdot \mathbf{a}_j) = \sum_i q_i (2\pi \delta_{ij}) = 2\pi q_j. \quad (\text{A.9})$$

Eqs. (A.7) and (A.8) become

$$\Delta E_{\mathbf{Q}}^{123} = J_1 - \frac{J_2}{2} \cos(2\pi q_1) - J_3 \cos(\pi q_1) \cos[\pi(2q_2 - q_1)], \quad (\text{A.10})$$

$$\Delta E_{\mathbf{Q}}^{124} = J_1 - \frac{J_2}{2} \cos(2\pi q_1) - \frac{J_4}{2} \cos[2\pi(q_3 - q_1)]. \quad (\text{A.11})$$

2. Dynamical structure factor

We denote the ground state by $|\Psi_g\rangle$ and its energy eigenvalue by E_g . We also denote the basis of the subspace of wavevectors \mathbf{Q} by $\{|\lambda_{\mathbf{Q}}\rangle\}$. Let these be eigenstates of H with energy eigenvalues $E_{\lambda_{\mathbf{Q}}}$. Then, the dynamical structure factor $\mathcal{S}^{+-}(\mathbf{Q}, \omega)$ at $T = 0$ can be written as

$$\mathcal{S}^{+-}(\mathbf{Q}, \omega) = \sum_{\lambda_{\mathbf{Q}}} |\langle \lambda_{\mathbf{Q}} | S_{\mathbf{Q}}^+ | \Psi_g \rangle|^2 \delta(\omega - E_{\lambda_{\mathbf{Q}}} + E_g).$$

The spin operator $S_{\mathbf{Q}}^+$ on the right-hand side is defined by

$$S_{\mathbf{Q}}^+ = \frac{1}{\sqrt{2N}} \sum_{i,\nu} e^{i\mathbf{Q} \cdot (\mathbf{r}_i + \mathbf{d}_{\nu})} S_{i,\nu}^+,$$

where $2N$ represents the total number of spins, \mathbf{r}_i represents the position of the i -th dimer, and $\mathbf{r}_i + \mathbf{d}_{\nu}$ represents the position of the spin $S_{i,\nu}$.

Let the ground state $|\Psi_g\rangle = |s\rangle$. Then, we need to evaluate

$$S_{\mathbf{Q}}^+ |s\rangle = \frac{1}{\sqrt{2N}} \sum_{i,\nu} e^{i\mathbf{Q} \cdot (\mathbf{r}_i + \mathbf{d}_{\nu})} S_{i,\nu}^+ |s\rangle. \quad (\text{A.12})$$

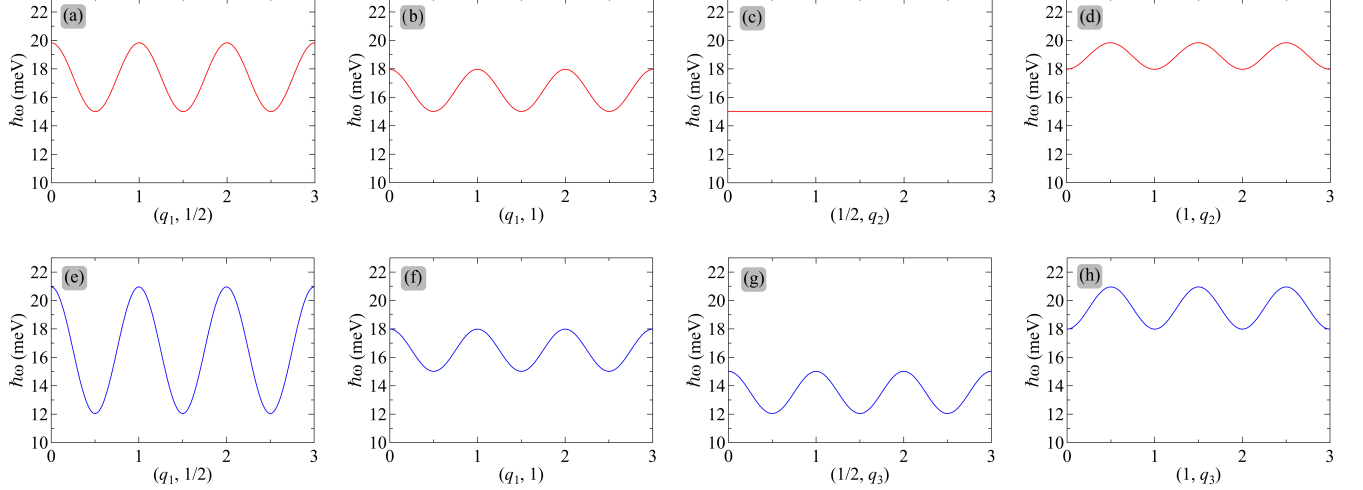


FIG. 8. (a)-(d) Dispersions along q_1 and q_2 directions for the J_1 - J_2 - J_3 model calculated with $J_1 = 16.95$ meV, $J_2 = -3.9$ meV, and $J_3 = 0.9$ meV. (e)-(h) Dispersions along q_1 and q_3 directions for the J_1 - J_2 - J_4 model calculated with $J_1 = 16.5$ meV, $J_2 = -6$ meV, and $J_4 = 3$ meV.

Noting that

$$\begin{aligned} S_{i,\nu}^+ |s\rangle &= S_{i,\nu}^+ |s\rangle_i \prod_{j(\neq i)} |s\rangle_j \\ &= (-1)^{\nu+1} |t_i^+\rangle \prod_{j(\neq i)} |s\rangle_j \\ &= (-1)^{\nu+1} |t_i^+\rangle, \end{aligned}$$

we find Eq.(A.12) can be written as

$$\begin{aligned} S_{\mathbf{Q}}^+ |s\rangle &= \frac{1}{\sqrt{2N}} \sum_{i,\nu} e^{i\mathbf{Q}\cdot(\mathbf{r}_i+\mathbf{d}_\nu)} (-1)^{\nu+1} |t_i^+\rangle \\ &= \frac{1}{\sqrt{2}} \sum_{\nu} e^{i\mathbf{Q}\cdot\mathbf{d}_\nu} (-1)^{\nu+1} |t_{\mathbf{Q}}^+\rangle, \end{aligned} \quad (\text{A.13})$$

where

$$|t_{\mathbf{Q}}^+\rangle = \frac{1}{\sqrt{N}} \sum_i |t_i^+\rangle e^{i\mathbf{Q}\cdot\mathbf{r}_i}.$$

From Eq. (A.13) we can see that matrix elements appear only when $|\lambda_Q\rangle = |t_Q^+\rangle$. Therefore, $\mathcal{S}^{+-}(\mathbf{Q}, \omega)$ can be written as

$$\mathcal{S}^{+-}(\mathbf{Q}, \omega) = |\langle t_Q^+ | S_{\mathbf{Q}}^+ | s \rangle|^2 \delta(\omega - \Delta E_{\mathbf{Q}}).$$

The matrix element $\langle t_Q^+ | S_{\mathbf{Q}}^+ | s \rangle$ is

$$\langle t_Q^+ | S_{\mathbf{Q}}^+ | s \rangle = \frac{1}{\sqrt{2}} \sum_{\nu} e^{i\mathbf{Q}\cdot\mathbf{d}_\nu} (-1)^{\nu+1}$$

and taking the square of the absolute value,

$$\begin{aligned} |\langle t_Q^+ | S_{\mathbf{Q}}^+ | s \rangle|^2 &= \left| \frac{1}{\sqrt{2}} \sum_{\nu} e^{i\mathbf{Q}\cdot\mathbf{d}_\nu} (-1)^{\nu+1} \right|^2 \\ &= \frac{1}{2} (e^{i\mathbf{Q}\cdot\mathbf{d}_0} - e^{i\mathbf{Q}\cdot\mathbf{d}_1}) (e^{-i\mathbf{Q}\cdot\mathbf{d}_0} - e^{-i\mathbf{Q}\cdot\mathbf{d}_1}) \\ &= 1 - \cos[\mathbf{Q} \cdot (\mathbf{d}_1 - \mathbf{d}_0)]. \end{aligned}$$

Noting that $\mathbf{d}_1 - \mathbf{d}_0 = \frac{2}{3}\mathbf{a}_1$ for both models, we thus have

$$\mathbf{Q} \cdot (\mathbf{d}_1 - \mathbf{d}_0) = \frac{4\pi}{3} q_1,$$

and

$$|\langle t_Q^+ | S_{\mathbf{Q}}^+ | s \rangle|^2 = 1 - \cos\left(\frac{4\pi}{3} q_1\right).$$

Therefore, the expression for the dynamical structure factor can be written as

$$\mathcal{S}^{+-}(\mathbf{Q}, \omega) = \left[1 - \cos\left(\frac{4\pi}{3} q_1\right) \right] \delta(\omega - \Delta E_{\mathbf{Q}}). \quad (\text{A.14})$$

[1] S. Sachdev, Quantum magnetism and criticality, *Nature Physics* **4**, 173 (2008), 0711.3015.
[2] A. Vasiliev, O. Volkova, E. Zvereva, and M. Markina, Milestones of low-D quantum magnetism, *npj Quantum*

Materials

[3] T. Nikuni, M. Oshikawa, A. Oosawa, and H. Tanaka, Bose-Einstein Condensation of Dilute Magnons in TiCuCl_3 , *Physical Review Letters* **84**, 5868 (1999), cond-

mat/9908118.

[4] C. Rüegg, N. Cavadini, A. Furrer, H. U. Gudel, K. Kramer, H. Mutka, A. Wildes, K. Habicht, and P. Vorderwisch, Bose-Einstein condensation of the triplet states in the magnetic insulator $TlCuCl_3$, *Nature* **423**, 62 (2003).

[5] M. Jaime, V. F. Correa, N. Harrison, C. D. Batista, N. Kawashima, Y. Kazuma, G. A. Jorge, R. Stern, I. Heinmaa, S. A. Zvyagin, Y. Sasago, and K. Uchinokura, Magnetic-Field-Induced Condensation of Triplons in Han Purple Pigment $BaCuSi_2O_6$, *Physical Review Letters* **93**, 087203 (2004), cond-mat/0404324.

[6] V. S. Zapf, D. Zocco, B. R. Hansen, M. Jaime, N. Harrison, C. D. Batista, M. Kenzelmann, C. Niedermayer, A. Lacerda, and A. Paduan-Filho, Bose-Einstein Condensation of $S = 1$ Nickel Spin Degrees of Freedom in $NiCl_2$ -4SC(NH₂)₂, *Physical Review Letters* **96**, 077204 (2006), cond-mat/0505562.

[7] T. Giamarchi, C. Rüegg, and O. Tchernyshyov, Bose-Einstein condensation in magnetic insulators, *Nature Physics* **4**, 198 (2008), 0712.2250.

[8] A. A. Aczel, Y. Kohama, C. Marcenat, F. Weickert, M. Jaime, O. E. Ayala-Valenzuela, R. D. McDonald, S. D. Selesnic, H. A. Dabkowska, and G. M. Luke, Field-Induced Bose-Einstein Condensation of Triplons up to 8 K in $Sr_3Cr_2O_8$, *Physical Review Letters* **103**, 207203 (2009), 0908.3049.

[9] V. Zapf, M. Jaime, and C. D. Batista, Bose-Einstein condensation in quantum magnets, *Reviews of Modern Physics* **86**, 563 (2014).

[10] E. C. Samulon, Y. Kohama, R. D. McDonald, M. C. Shapiro, K. A. Al-Hassanieh, C. D. Batista, M. Jaime, and I. R. Fisher, Asymmetric Quintuplet Condensation in the Frustrated $S = 1$ Spin Dimer Compound $Ba_3Mn_2O_8$, *Physical Review Letters* **103**, 047202 (2009), 0905.0467.

[11] S. E. Sebastian, N. Harrison, C. D. Batista, L. Balicas, M. Jaime, P. A. Sharma, N. Kawashima, and I. R. Fisher, Dimensional reduction at a quantum critical point, *Nature* **441**, 617 (2006), cond-mat/0606042.

[12] C. Rüegg, B. Normand, M. Matsumoto, A. Furrer, D. F. McMorrow, K. W. Krämer, H. U. Gudel, S. N. Gvasaliya, H. Mutka, and M. Boehm, Quantum Magnets under Pressure: Controlling Elementary Excitations in $TlCuCl_3$, *Physical Review Letters* **100**, 205701 (2008), 0803.3720.

[13] P. A. McClarty, F. Krüger, T. Guidi, S. F. Parker, K. Refson, A. W. Parker, D. Prabhakaran, and R. Coldea, Topological triplon modes and bound states in a Shastry-Sutherland magnet, *Nature Physics* **13**, 736 (2017).

[14] A. Koga and N. Kawakami, Quantum Phase Transitions in the Shastry-Sutherland Model for $SrCu_2(BO_3)_2$, *Physical Review Letters* **84**, 4461 (2000), cond-mat/0003435.

[15] M. E. Zayed, C. Rüegg, J. L. J., A. M. Läuchli, C. Panagopoulos, S. S. Saxena, M. Ellerby, D. F. McMorrow, T. Strässle, S. Klotz, G. Hamel, R. A. Sadykov, V. Pomjakushin, M. Boehm, M. Jiménez-Ruiz, A. Schneidewind, E. Pomjakushina, M. Stingaciu, K. Conder, and H. M. Rønnow, 4-spin plaque-tte singlet state in the Shastry-Sutherland compound $SrCu_2(BO_3)_2$, *Nature Physics* **13**, 962 (2017), 1603.02039.

[16] E. Fogh, M. Nayak, O. Prokhnenco, M. Bartkowiak, K. Munakata, J.-R. Soh, A. A. Turrini, M. E. Zayed, E. Pomjakushina, H. Kageyama, H. Nojiri, K. Kakurai, B. Normand, F. Mila, and H. M. Rønnow, Field-induced bound-state condensation and spin-nematic phase in $SrCu_2(BO_3)_2$ revealed by neutron scattering up to 25.9 T, *Nature Communications* **15**, 442 (2024), 2306.07389.

[17] M. Takigawa, M. Horvatić, T. Waki, S. Krämer, C. Berthier, F. Lévy-Bertrand, I. Sheikin, H. Kageyama, Y. Ueda, and F. Mila, Incomplete Devil's Staircase in the Magnetization Curve of $SrCu_2(BO_3)_2$, *Physical Review Letters* **110**, 067210 (2013), 1209.0069.

[18] P. Corboz and F. Mila, Crystals of Bound States in the Magnetization Plateaus of the Shastry-Sutherland Model, *Physical Review Letters* **112**, 147203 (2014), 1401.3778.

[19] D. A. Tennant, B. Lake, A. J. A. James, F. H. L. Essler, S. Notbohm, H.-J. Mikeska, J. Fielden, P. Kögerler, P. C. Canfield, and M. T. F. Telling, Anomalous dynamical line shapes in a quantum magnet at finite temperature, *Physical Review B* **85**, 014402 (2012).

[20] E. S. Klyushina, A. T. M. N. Islam, J. T. Park, E. A. Goremychkin, E. Wheeler, B. Klemke, and B. Lake, Hamiltonian of the $S = \frac{1}{2}$ dimerized antiferromagnetic-ferromagnetic quantum spin chain $BaCu_2V_2O_8$, *Physical Review B* **98**, 104413 (2018).

[21] K. Kodama, H. Harashina, H. Sasaki, M. Kato, M. Sato, K. Kakurai, and M. Nishi, Neutron Scattering Study on the Quasi-One-Dimensional Spin-Gap System $CuNb_2O_6$, *Journal of the Physical Society of Japan* **68**, 237 (1999).

[22] M. B. Stone, W. Tian, M. D. Lumsden, G. E. Granroth, D. Mandrus, J.-H. Chung, N. Harrison, and S. E. Nagler, Quantum Spin Correlations in an Organometallic Alternating-Sign Chain, *Physical Review Letters* **99**, 087204 (2007), 0705.0523.

[23] K. Momma and F. Izumi, *VESTA3* for three-dimensional visualization of crystal, volumetric and morphology data, *Journal of Applied Crystallography* **44**, 1272 (2011).

[24] Y. Miura, R. Hirai, Y. Kobayashi, and M. Sato, Spin-Gap Behavior of $Na_3Cu_2SbO_6$ with Distorted Honeycomb Structure, *Journal of the Physical Society of Japan* **75**, 084707 (2006).

[25] Y. Miura, Y. Yasui, T. Moyoshi, M. Sato, and K. Kakurai, Magnetic Excitations of Spin-Gap System $Na_3Cu_2SbO_6$ with Distorted Honeycomb Structure, *Journal of the Physical Society of Japan* **77**, 104709 (2008).

[26] H.-J. Koo and M.-H. Whangbo, Analysis of the Spin Lattice Model for the Spin-Gapped Layered Compounds $Na_3Cu_2SbO_6$ and $Na_2Cu_2TeO_6$ on the Basis of Electronic Structure Calculations, *Inorganic Chemistry* **47**, 128 (2008).

[27] C. Kuo, T. Jian, and C. Lue, Characterization of the spin gap nature in $Na_3Cu_2SbO_6$ using ²³Na NMR, *Journal of Alloys and Compounds* **531**, 1 (2012).

[28] M. Schmitt, O. Janson, S. Golbs, M. Schmidt, W. Schnelle, J. Richter, and H. Rosner, Microscopic magnetic modeling for the $S = \frac{1}{2}$ alternating-chain compounds $Na_3Cu_2SbO_6$ and $Na_2Cu_2TeO_6$, *Physical Review B* **89**, 174403 (2014).

[29] C. Koo, E. A. Zvereva, I. L. Shukaev, M. Richter, M. I. Stratan, A. N. Vasiliev, V. B. Nalbandyan, and R. Klingeler, Static and Dynamic Magnetic Response of Fragmented Haldane-like Spin Chains in Layered $Li_3Cu_2SbO_6$, *Journal of the Physical Society of Japan* **85**, 084702 (2016).

[30] E. Vavilova, S. Nishimoto, T. Salikhov, T. Vasilchikova, V. Nalbandyan, A. Vasiliev, and E. Zvereva, Spin dynamics in the alternating chain system $\text{Li}_3\text{Cu}_2\text{SbO}_6$ with defects probed by nuclear magnetic resonance, *Physical Review B* **103**, 094415 (2021).

[31] S. Gao, L.-F. Lin, A. F. May, B. K. Rai, Q. Zhang, E. Dagotto, A. D. Christianson, and M. B. Stone, Weakly coupled alternating $S = 1/2$ chains in the distorted honeycomb lattice compound $\text{Na}_2\text{Cu}_2\text{TeO}_6$, *Physical Review B* **102**, 220402 (2020).

[32] Y. Shangguan, S. Bao, Z.-Y. Dong, Z. Cai, W. Wang, Z. Huang, Z. Ma, J. Liao, X. Zhao, R. Kajimoto, K. Iida, D. Voneshen, S.-L. Yu, J.-X. Li, and J. Wen, Evidence for strong correlations at finite temperatures in the dimerized magnet $\text{Na}_2\text{Cu}_2\text{TeO}_6$, *Physical Review B* **104**, 224430 (2021).

[33] L.-F. Lin, R. Soni, Y. Zhang, S. Gao, A. Moreo, G. Alvarez, A. D. Christianson, M. B. Stone, and E. Dagotto, Electronic structure, magnetic properties, and pairing tendencies of the copper-based honeycomb lattice $\text{Na}_2\text{Cu}_2\text{TeO}_6$, *Physical Review B* **105**, 245113 (2022).

[34] J. Skakle, M. C. R., S. Tovar, and A. West, Synthesis of $\text{Li}_3\text{Cu}_2\text{SbO}_6$, a New Partially Ordered Rock Salt Structure, *Journal of Solid State Chemistry* **131**, 115 (1997).

[35] V. Nalbandyan, M. Avdeev, and M. Evstigneeva, Crystal structure of $\text{Li}_4\text{ZnTeO}_6$ and revision of $\text{Li}_3\text{Cu}_2\text{SbO}_6$, *Journal of Solid State Chemistry* **199**, 62 (2013).

[36] V. Kumar, A. Gupta, and S. Uma, Formation of honeycomb ordered monoclinic $\text{Li}_2\text{M}_2\text{TeO}_6$ ($\text{M} = \text{Cu, Ni}$) and disordered orthorhombic $\text{Li}_2\text{Ni}_2\text{TeO}_6$ oxides, *Dalton Transactions* **42**, 14992 (2013).

[37] O. Smirnova, V. Nalbandyan, A. Petrenko, and M. Avdeev, Subsolidus phase relations in $\text{Na}_2\text{O}-\text{CuO}-\text{Sb}_2\text{O}_n$ system and crystal structure of new sodium copper antimonate $\text{Na}_3\text{Cu}_2\text{SbO}_6$, *Journal of Solid State Chemistry* **178**, 1165 (2005).

[38] J. Xu, A. Assoud, N. Soheilnia, S. Derakhshan, H. L. Cuthbert, J. E. Greedan, M. H. Whangbo, and H. Kleinke, Synthesis, Structure, and Magnetic Properties of the Layered Copper(II) Oxide $\text{Na}_2\text{Cu}_2\text{TeO}_6$, *Inorganic Chemistry* **44**, 5042 (2005).

[39] R. Sankar, I. P. Muthuselvam, G. J. Shu, W. T. Chen, S. K. Karna, R. Jayavel, and F. C. Chou, Crystal growth and magnetic ordering of $\text{Na}_2\text{Ni}_2\text{TeO}_6$ with honeycomb layers and $\text{Na}_2\text{Cu}_2\text{TeO}_6$ with Cu spin dimers, *CrystEngComm* **16**, 10791 (2014).

[40] T. Murtaza, R. Kalaivanan, G. Madeswaran, K. Bayikadi, and R. Sankar, Magnetic properties of honeycomb spin lattice compounds $\text{Na}_2\text{M}_2\text{TeO}_6$ ($\text{M} = \text{Co, Ni}$) and spin dimer compound $\text{Na}_2\text{Cu}_2\text{TeO}_6$ single crystals by flux-growth, *Journal of Materials Research and Technology* **14**, 1601 (2021).

[41] K. Morimoto, Y. Itoh, K. Yoshimura, M. Kato, and K. Hirota, Hole Doping Effects on Spin-gapped $\text{Na}_2\text{Cu}_2\text{TeO}_6$ via Topochemical Na Deficiency, *Journal of the Physical Society of Japan* **75**, 083709 (2006), cond-mat/0607141.

[42] S. Derakhshan, H. L. Cuthbert, J. E. Greedan, B. Rahaman, and T. Saha-Dasgupta, Electronic structures and low-dimensional magnetic properties of the ordered rock-salt oxides $\text{Na}_3\text{Cu}_2\text{SbO}_6$ and $\text{Na}_2\text{Cu}_2\text{TeO}_6$, *Physical Review B* **76**, 104403 (2007).

[43] S. Patil and S. D. Kaushik, Investigating structure and physical properties of quaternary layered transition metal oxide $\text{Na}_2\text{Cu}_2\text{TeO}_6$, arXiv 10.48550/arxiv.2508.16219 (2025), 2508.16219.

[44] P. W. Anderson, Antiferromagnetism. Theory of Superexchange Interaction, *Physical Review* **79**, 350 (1950).

[45] J. B. Goodenough, Theory of the Role of Covalence in the Perovskite-Type Manganites $[\text{La, M(II)}]\text{MnO}_3$, *Physical Review* **100**, 564 (1955).

[46] J. B. Goodenough, An interpretation of the magnetic properties of the perovskite-type mixed crystals $\text{La}_{1-x}\text{Sr}_x\text{CoO}_{3-\lambda}$, *Journal of Physics and Chemistry of Solids* **6**, 287 (1958).

[47] A. S. Moskvin, N. S. Ovanesyan, and V. A. Trukhtanov, Angular dependence of the superexchange interaction $\text{Fe}^{3+}-\text{O}^{2-}-\text{Cr}^{3+}$, *Hyperfine Interactions* **1**, 265 (1975).

[48] E. Climent-Pascual, P. Norby, N. H. Andersen, P. W. Stephens, H. W. Zandbergen, J. Larsen, and R. J. Cava, Spin 1/2 Delafossite Honeycomb Compound Cu_5SbO_6 , *Inorganic Chemistry* **51**, 557 (2011).

[49] P. Sae-Fu, et al. (2025), manuscript in preparation.

[50] K. Nakajima, S. Ohira-Kawamura, T. Kikuchi, M. Nakamura, R. Kajimoto, Y. Inamura, N. Takahashi, K. Aizawa, K. Suzuya, K. Shibata, T. Nakatani, K. Soyama, R. Maruyama, H. Tanaka, W. Kambara, T. Iwashashi, Y. Itoh, T. Osakabe, S. Wakimoto, K. Kakurai, F. Maekawa, M. Harada, K. Oikawa, R. E. Lechner, F. Mezei, and M. Arai, AMATERAS: A Cold-Neutron Disk Chopper Spectrometer, *Journal of the Physical Society of Japan* **80**, SB028 (2011).

[51] J. W. Lynn, Y. Chen, S. Chang, Y. Zhao, S. Chi, W. Ratcliff, B. G. Ueland, and R. W. Erwin, Double-Focusing Thermal Triple-Axis Spectrometer at the NCNR, *Journal of Research of the National Institute of Standards and Technology* **117**, 61 (2012).

[52] Y. Inamura, T. Nakatani, J. Suzuki, and T. Otomo, Development Status of Software “Utsusemi” for Chopper Spectrometers at MLF, J-PARC, *Journal of the Physical Society of Japan* **82**, SA031 (2013).

[53] V. Petříček, M. Dušek, and L. Palatinus, Crystallographic computing system *jana2006*: General features, *Zeitschrift für Kristallographie - Crystalline Materials* **229**, 345 (2014).

[54] H. M. Rietveld, A profile refinement method for nuclear and magnetic structures, *Journal of Applied Crystallography* **2**, 65 (1969).

[55] J. Rodríguez-Carvajal, Recent advances in magnetic structure determination by neutron powder diffraction, *Physica B: Condensed Matter* **192**, 55 (1993).

[56] B. Ravel and M. Newville, *ATHENA*, *ARTEMIS*, *HEP-HAESTUS*: data analysis for x-ray absorption spectroscopy using *IFEFFIT*, *Journal of Synchrotron Radiation* **12**, 537 (2005).

[57] M. Newville, Fundamentals of XAFS, *Reviews in Mineralogy and Geochemistry* **78**, 33 (2014).

[58] J. Bréger, M. Jiang, N. Dupré, Y. S. Meng, Y. Shao-Horn, G. Ceder, and C. P. Grey, High-resolution X-ray diffraction, DIFFaX, NMR and first principles study of disorder in the $\text{Li}_2\text{MnO}_3-\text{Li}[\text{Ni}_{1/2}\text{Mn}_{1/2}]\text{O}_2$ solid solution, *Journal of Solid State Chemistry* **178**, 2575 (2005).

[59] S. K. Choi, R. Coldea, A. N. Kolmogorov, T. Lancaster, I. I. Mazin, S. J. Blundell, P. G. Radaelli, Y. Singh, P. Gegenwart, K. R. Choi, S.-W. Cheong, P. J. Baker, C. Stock, and J. Taylor, Spin Waves and Revised Crystal Structure of Honeycomb Iridate Na_2IrO_3 , *Physical Review Letters* **108**, 127204 (2012), 1202.1268.

[60] M. M. J. Treacy, J. M. Newsam, and M. W. Deem, A general recursion method for calculating diffracted intensities from crystals containing planar faults, *Proceedings of the Royal Society of London. Series A: Mathematical and Physical Sciences* **433**, 499 (1991).

[61] M. Casas-Cabanas, J. Rodríguez-Carvajal, and M. Palacín, Faults, a new program for refinement of powder diffraction patterns from layered structures, in *Ninth European Powder Diffraction Conference* (Oldenbourg Wissenschaftsverlag, München, 2006) pp. 243–248.

[62] M. Casas-Cabanas, M. Reynaud, J. Rikarte, P. Horbach, and J. Rodríguez-Carvajal, *FAULTS*: a program for refinement of structures with extended defects, *Journal of Applied Crystallography* **49**, 2259 (2016).

[63] S. Todo and K. Kato, Cluster Algorithms for General- S Quantum Spin Systems, *Physical Review Letters* **87**, 047203 (2001).

[64] H. G. Evertz, The loop algorithm, *Advances in Physics* **52**, 1 (2003).

[65] B. Bauer, L. D. Carr, H. G. Evertz, A. Feiguin, J. Freire, S. Fuchs, L. Gamper, J. Gukelberger, E. Gull, S. Guertler, A. Hehn, R. Igarashi, S. V. Isakov, D. Koop, P. N. Ma, P. Mates, H. Matsuo, O. Parcollet, G. Pawłowski, J. D. Picon, L. Pollet, E. Santos, V. W. Scarola, U. Schollwöck, C. Silva, B. Surer, S. Todo, S. Trebst, M. Troyer, M. L. Wall, P. Werner, and S. Wessel, The ALPS project release 2.0: open source software for strongly correlated systems, *Journal of Statistical Mechanics: Theory and Experiment* **2011**, P05001 (2011).

[66] D. C. Johnston, R. K. Kremer, M. Troyer, X. Wang, A. Klümper, S. L. Bud'ko, A. F. Panchula, and P. C. Canfield, Thermodynamics of spin $S = 1/2$ antiferromagnetic uniform and alternating-exchange Heisenberg chains, *Physical Review B* **61**, 9558 (2000), cond-mat/0003271.

[67] O. F. Syljuåsen and A. W. Sandvik, Quantum Monte Carlo with directed loops, *Physical Review E* **66**, 046701 (2002), cond-mat/0202316.

[68] O. F. Syljuåsen, Directed loop updates for quantum lattice models, *Physical Review E* **67**, 046701 (2003), cond-mat/0211513.

[69] G. Xu, C. L. Broholm, Y.-A. Soh, G. Aeppli, J. F. Ditusa, Y. Chen, M. Kenzelmann, C. D. Frost, T. Ito, K. Oka, and H. Takagi, Mesoscopic phase coherence in a quantum spin fluid, *Science* **317**, 1049 (2007).

[70] F. H. L. Essler and R. M. Konik, Finite-temperature line-shapes in gapped quantum spin chains, *Physical Review B* **78**, 100403 (2008), 0711.2524.

[71] I. Exius, K. P. Schmidt, B. Lake, D. A. Tennant, and G. S. Uhrig, Vertex corrections in the dynamic structure factor in spin ladders, *Physical Review B* **82**, 214410 (2010), 1010.2459.

[72] B. Normand and C. Rüegg, Complete bond-operator theory of the two-chain spin ladder, *Physical Review B* **83**, 054415 (2011), 1006.4196.

[73] F. Verstraete, M. Popp, and J. I. Cirac, Entanglement versus Correlations in Spin Systems, *Physical Review Letters* **92**, 027901 (2003), quant-ph/0307009.

[74] B.-Q. Jin and V. E. Korepin, Localizable entanglement in antiferromagnetic spin chains, *Physical Review A* **69**, 062314 (2004).

[75] Č. Brukner, V. Vedral, and A. Zeilinger, Crucial role of quantum entanglement in bulk properties of solids, *Physical Review A* **73**, 012110 (2006), quant-ph/0410138.